Charles University in Prague
Faculty of Mathematics and Physics

Master Thesis

Jan Burjánek

A composite source model with fractal subevent size distribution

Supervisor: Doc. RNDr. Jiří Zahradník, DrSc.

Department of Geophysics
Prague, 2002

Acknowledgements

First of all, I want to thank Doc. RNDr. Jiří Zahradník, DrSc., the supervisor of my master thesis, for priceless advice and valuable comments that helped me solve many problems. I would like to thank my parents for the patience and help during my studies.

Number of figures was made with Generic Mapping Tools (Wessel and Smith (1991)). The author was supported by the following grants: NATO Collaborative Linkage Grant EST.CLG.976035, EU project EVG1-CT-1999-00001 PRESAP and several research projects in the Czech Republic - MSMT DG MSM/98-113200004, GACR 205/00/0902 and GAUK 176/2000/B GEO/MFF.

Prohlašuji, že jsem svou diplomovou práci napsal samostatně a výhradně s použitím citovaných pramenů. Souhlasím se zapůjčováním práce.

V Praze dne 19.4.2002 Jan Burjánek

Název práce: A composite source model with fractal subevent size distribution
Autor: Jan Burjánek
Katedra: Katedra geofyziky
Vedoucí diplomové práce: Doc. RNDr. Jiří Zahradník, DrSc.
e-mail vedoucího: jz@karel.troja.mff.cuni.cz

Abstrakt: Kompozitní model, který bere v úvahu různě velké elementární zdroje, představuje jeden z možných popisů seismického zdroje. Počet elementárních zdrojů s velikostí větší než R je úměrný R^{-2}. Elementární zdroje se nepřekrývají a jejich celková plocha má stejný obsah jako zlomová plocha hlavního otřesu. Rozložení elementárních zdrojů na hlavní zlomové ploše je náhodné. Elementární zdroje jsou modelovány bud' jako konečné zdroje, a to konkrétně kinematicky (radiální šíření trhliny s konstantní rychlostí, skluzová funkce je funkce typu rampa s náběhovým časem rovným době trhání), nebo v bodovém přiblížení. Hodnota konečného skluzu na elementárním zdroji je úměrná velikosti elementárního zdroje. Syntetické Greenovy funkce se počítají metodou diskrétních vlnových čísel v 1D vrstevnatém prostředí v relativně řídké síti bodů. Greenovy funkce v husté síti bodů se dostávají za použití interpolace (kubické splajny). Výše popsaný kompozitní model je možné interpretovat jako kinematický model s nerovnoměrným rozložením skluzu a s nerovnoměrným časem příchodu trhliny. Metoda byla aplikována při modelování silných pohybů půdy způsobených Aténským zemětřesením 1999 (Mw=5.9).

Klíčová slova: kompozitní modelování zdroje, fraktály, k^{-2} skluz, silné pohyby půdy

Title: A composite source model with fractal subevent size distribution
Author: Jan Burjánek
Department: Dept. of Geophysics
Supervisor: Doc. RNDr. Jiří Zahradník, DrSc.
Supervisor's e-mail address: jz@karel.troja.mff.cuni.cz

Abstract: A composite source model, incorporating different sized subevents, provides a possible description of complex rupture processes during earthquakes. The number of subevents with characteristic dimension greater than R is proportional to R^{-2}. The subevents do not overlap with each other, and the sum of their areas equals to the area of the target event (e.g. mainshock) . The subevents are distributed randomly over the fault. Each subevent is modelled either as a finite source, using kinematic approach (radial rupture propagation, constant rupture velocity, boxcar slip-velocity function, with constant rise time on the subevent) or as a point source. The final slip at each subevent is related to its characteristic dimension, using constant stress-drop scaling. The synthetic Green's functions are calculated by the discrete-wavenumber method in a 1D horizontally layered crustal model in a relatively coarse grid of points covering the fault plane. The Green's functions in a fine grid are obtained by cubic spline interpolation. The composite source model described above allows interpretation in terms of a kinematic model with non-uniform final slip and rupture velocity spatial distributions. The strong ground motion modelling of the 1999 Athens earthquake ($M_w = 5.9$) was performed.

Keywords: composite source modelling, fractals, k^{-2} slip, strong ground motion

Contents

Chapter 1

Introduction

Accurate estimation of strong ground motion in a broad-frequency band (0.5-20 Hz) for future large earthquakes is one of the major topics of present strong motion seismology. Syntheses of strong ground motion are based on combination of generation (source effects) and propagation of seismic waves in Earth. The problem is, that at high frequencies ($f \sim 20\,Hz$) deterministic methods based on limited knowledge of Earth's interior still fail. The problems adherent to propagation effects are quite obvious, present crustal models are insufficient for such high frequencies. The problems adherent to source effects are may be even more complicated, because there has not been developed yet universal physical theory of faulting processes.

This thesis is particularly focused on the modelling of finite-extent sources. Seismic sources are of course studied in various ways. We mention here three main approaches: dynamic modelling, kinematic modelling and composite modelling of seismic source. The goal of dynamic modelling of seismic source is to determine point of rupture initiation, rupture velocity and slip behavior over the fault, from stress acting on the fault, strength of the fault and properties of material surrounding the fault (see Kostrov and Das (1988)). One can see, that dynamic modelling represents very complex problem by itself, and therefore it is not suitable for strong ground motions simulations. On the other hand kinematic modelling of seismic source represents favorable choice from strong ground motion point of view. The problem of seismic source is reduced to specification of the dislocation on a fault as a function of time and position (usually expressed in form of representation theorem presented by Aki and Richards (1980)). In other words kinematic modelling of seismic source starts at the point, where dynamic modelling of seismic source usually results. The composite modelling of seismic source represents quite different approach. The seismic source is taken as a case of certain self-similar entity. In other words, seismic source is assumed to be composed from smaller seismic sources (usually called subevents). The idea of composite source model came from EGF (Empirical Green's Function) method, where time history of mainshock is built up from aftershocks (Hartzell (1978)). In

this study we are going to enhance recent composite source models by incorporating non-equal sized subevents. Although composite models with non-equal sized subevents were already studied from both theoretical (Boatwright (1982), Frankel (1991)) and practical (Zeng et al. (1994), Irikura and Kamae (1994), Hartzell et al. (1999)) points of view, the number of uncertainties and uncompleted descriptions does not allow to use these models universally. So that the motivation for this study was to build up composite model, which would be simple, universal and which would be without any contradictory assumptions. Chapter 2 provides description of composite source model with equal sizes to show basic properties of composite modelling. Then in Chapter 3, which represents the fundamental part of this master thesis, non-equal sized subevents are incorporated. In Chapter 4 we outline possible ways of subevents modelling and finally in Chapter 5 there is shown an example application of developed composite model for Athens 1999 earthquake.

Chapter 2

Subevents with equal sizes

2.1 Scaling laws

Scaling laws between large and small earthquakes have to be considered for building composite source model. Set of scaling laws for source parameters such as fault area, average final slip and scalar seismic moment, introduced by Kanamori and Anderson (1975) and assuming constant stress drop are

$$\frac{L^m}{L^s} = \frac{W^m}{W^s} = \frac{\langle u \rangle^m}{\langle u \rangle^s} = \frac{f_c^s}{f_c^m} = \left(\frac{M_o^m}{M_o^s} \right)^{\frac{1}{3}} = K \tag{2.1}$$

where L, W denote length, width of fault area, $\langle u \rangle$, f_c, M_o, denote average final slip, corner frequency and scalar seismic moment respectively and K is constant. Superscripts m and s distinguish 2 different earthquakes. Present composite models, which have incorporated these laws, produce reasonable results (see Irikura and Kamae (1994), Frankel (1995), Hartzell et al. (1999)), however they aren't certain for wide magnitude ranges (see Mai and Beroza (2000)). In further study we will use the assumption of constant stress drop (2.1) to simplify derived formulas. A more general case of nonconstant stress drop can be found in Irikura and Kamae (1994).

2.2 ω^{-2} source model

Another fundamental assumption of presented composite model is f^{-2} falloff of amplitude displacement spectra above corner frequency f_c. The shape $|u(f)|$ of amplitude displacement spectra is prescribed, following Brune (1970), as

$$|u\,(f)| \propto \frac{M_o}{1 + \left(\frac{f}{f_c} \right)^2} \tag{2.2}$$

One can see that (2.2) has plateau for $f < f_c$, particularly

$$|u\,(f \to 0)| \propto M_o \tag{2.3}$$

The shape of amplitude acceleration spectra $|\ddot{u}(f)|$ is then, derived multiplying (2.2) by f^2,

$$|\ddot{u}\,(f)| \propto \frac{M_o f^2}{1 + \left(\frac{f}{f_c}\right)^2} \tag{2.4}$$

(2.4) has plateau for $f > f_c$, particularly

$$|\ddot{u}\,(f \to \infty)| \propto M_o f_c^2 \tag{2.5}$$

2.3 Summation method for subevents with equal sizes

The idea of ongoing study is to compose target event from smaller events, which meet (2.2), so as target event will meet (2.2), conserving (2.1).

Let's propose some basic assumptions about modelled event (i.e. mainshock): rupture fault is considered to be rectangle with known length L^m and width W^m, scalar seismic moment M_o^m, corner frequency f_c^m and mechanism are known parameters, too. Further, we assume that there are available seismograms of N subevents, which occur within the fault of the mainshock (i.e. mainfault). These subevents have same mechanism as the mainshock and appropriate rectangular subfault is assigned to each subevent. These subfaults fully fill up the mainfault. Moreover, we assume that all of these subevents have same moment M_o^s, corner frequency f_c^s and stress drop $\Delta\sigma$. Thus, due to constant stress drop scaling, all subfaults have same length L^s and width W^s. In other words, we simply cut the mainfault into N identical subfaults, so

$$\frac{L^m\,W^m}{L^s\,W^s} = N \tag{2.6}$$

The stress drop $\Delta\sigma$ is considered to be same for both mainshock and subevent, so by combination of (2.1) with (2.6), we obtain

$$\left(\frac{M_o^m}{M_o^s}\right)^{\frac{2}{3}} = N \tag{2.7}$$

One of the simplest ways how to build up the target event is to sum up contributions from subevents with appropriate time shift to model finite size of the mainfault, mathematically

$$\mathbf{\Omega}^{\Sigma}\,(t) = \sum_{m=1}^{N} \mathbf{\Omega}_m^s\,(t - t_m^r) \tag{2.8}$$

where $\mathbf{\Omega}^{\Sigma}(t)$ is modelled composite seismogram, $\mathbf{\Omega}_m^s(t)$ is contribution from m-th subevent, t_m^r is time, when the m-th subevent is initialized. Timing of subevents can be chosen in various ways, from completely random t_m^r (see Tumarkin (1994)), to t_m^r which follows prescribed rupture front spreading over mainfault (e.g. radial rupture). $\mathbf{\Omega}^{\Sigma}(t)$, $\mathbf{\Omega}_m^s(t)$ could be generally time histories of displacement, velocity or acceleration.

2.3.1 Summation process for random t_m^r

In this section, we are going to study general behavior of amplitude spectra $\left|\mathbf{\Omega}^{\Sigma}(f)\right|$ of simulated time history $\mathbf{\Omega}^{\Sigma}(t)$. Firstly, we show its asymptotic behavior, following Joyner and Boore (1986). In this case, it is useful to assume random subevent timing, to provide analytical derivation. Transforming (2.8) to frequency domain, we obtain

$$\mathbf{\Omega}^{\Sigma}(f) = \sum_{m=1}^{N} \mathbf{\Omega}_m^s(f)\, e^{-2\pi i f t_m^r} \tag{2.9}$$

It is clear that one realization of t_m^r and one set of $\mathbf{\Omega}_m^s(f)$ would not tell us much about the general shape of $\mathbf{\Omega}_m^{\Sigma}(f)$. Hence, we are going to study $\mathbf{\Omega}_m^{\Sigma}(f)$ statistically to provide trustful results. The *general shape* of $\mathbf{\Omega}_m^{\Sigma}(f)$ will be identified with *average* composite amplitude spectra and will be denoted $\left|\mathbf{\Omega}^{\Sigma}(f)\right|$. For the square of average amplitude spectra $\left|\mathbf{\Omega}^{\Sigma}(f)\right|$ we have

$$\left|\mathbf{\Omega}^{\Sigma}(f)\right|^2 = E_{\mathcal{T},\mathcal{S}}\left\{\left(\sum_{j=1}^{N} \mathbf{\Omega}_j^s(f)\, e^{-2\pi i f t_j^r}\right)\overline{\left(\sum_{k=1}^{N} \mathbf{\Omega}_k^s(f)\, e^{-2\pi i f t_k^r}\right)}\right\} \tag{2.10}$$

where $E_{\mathcal{T},\mathcal{S}}\{\ldots\}$ is operator of expectation (mean value, see Lee (1960)) from sets $\mathcal{T}$ and $\mathcal{S}$, bar over denotes complex conjugate, $\mathcal{T}$ denotes set of t_m^r, $\mathcal{S}$ denotes set of $\mathbf{\Omega}_m^s(f)$. Rearranging (2.10) we get

$$\left|\mathbf{\Omega}^{\Sigma}(f)\right|^2 = E_{\mathcal{T},\mathcal{S}}\left\{\sum_{j=1}^{N}\left[\overline{\mathbf{\Omega}_j^s(f)}\mathbf{\Omega}_j^s(f)\right] + \sum_{\substack{j,k=1\\ j\neq k}}^{N}\left[e^{-2\pi i f\left(t_j^r - t_k^r\right)}\overline{\mathbf{\Omega}_k^s(f)}\mathbf{\Omega}_j^s(f)\right]\right\} \tag{2.11}$$

We suppose that $\mathbf{\Omega}_j^s(f), \mathbf{\Omega}_k^s(f), t_j^r$ and t_k^r are independent of each other for $j \neq k$, thus

$$\begin{aligned}\left|\mathbf{\Omega}^{\Sigma}(f)\right|^2 = &\sum_{j=1}^{N}\left[E_{\mathcal{S}}\left\{\overline{\mathbf{\Omega}_j^s(f)}\mathbf{\Omega}_j^s(f)\right\}\right] \\ &+\sum_{\substack{j,k=1\\ j\neq k}}^{N}\left[E_{\mathcal{T}}\left\{e^{-2\pi i f\left(t_j^r-t_k^r\right)}\right\}E_{\mathcal{S}}\left\{\overline{\mathbf{\Omega}_k^s(f)}\mathbf{\Omega}_j^s(f)\right\}\right]\end{aligned} \tag{2.12}$$

As we supposed above, t_m^r is random variable, hence it can be described by certain probability density function $\rho(t_m^r)$. We choose simply uniform probability density function

$$\rho(t_m^r) = \begin{cases} 0 & t_m^r < 0 \\ \frac{1}{T} & 0 \leq t_m^r \leq T \\ 0 & t_m^r > T \end{cases} \tag{2.13}$$

where T is duration of the mainshock, which is inversely proportional to the corner frequency of the mainshock f_c^m. From definition of expectation $E\{\ldots\}$ we obtain

$$E\{f(t_m^r)\} = \int_{-\infty}^{\infty} f(t_m^r)\,\rho(t_m^r)\;dt_m^r = \frac{1}{T}\int_0^T f(t_m^r)\,dt_m^r \tag{2.14}$$

As we treat both t_k^r and t_j^r independently, $E_{\mathcal{T}}$ becomes

$$E_{\mathcal{T}}\left\{f\left(t_j^r\right)f(t_k^r)\right\} = \frac{1}{T^2}\int_0^T\int_0^T f\left(t_j^r\right)f(t_k^r)\,dt_j^r dt_k^r \tag{2.15}$$

Putting (2.15) into (2.12) we get

$$\begin{aligned}\left|\mathbf{\Omega}^{\Sigma}(f)\right|^2 = &\sum_{j=1}^{N}\left[E_{\mathcal{S}}\left\{\overline{\mathbf{\Omega}_j^s(f)}\mathbf{\Omega}_j^s(f)\right\}\right] \\ &+\frac{1}{T^2}\sum_{\substack{j,k=1\\ j\neq k}}^{N}\left[\int_0^T\int_0^T e^{-2\pi i f\left(t_j^r-t_k^r\right)}dt_j^r dt_k^r\;E_{\mathcal{S}}\left\{\overline{\mathbf{\Omega}_k^s(f)}\mathbf{\Omega}_j^s(f)\right\}\right]\end{aligned} \tag{2.16}$$

Obvious integration produces

$$\begin{aligned}\left|\mathbf{\Omega}^{\Sigma}(f)\right|^2 = &\sum_{j=1}^{N}\left[E_{\mathcal{S}}\left\{\overline{\mathbf{\Omega}_j^s(f)}\mathbf{\Omega}_j^s(f)\right\}\right] \\ &+\sum_{\substack{j,k=1\\ j\neq k}}^{N}\left[\operatorname{sinc}^2\left(\frac{fT}{2}\right)E_{\mathcal{S}}\left\{\overline{\mathbf{\Omega}_k^s(f)}\mathbf{\Omega}_j^s(f)\right\}\right]\end{aligned} \tag{2.17}$$

where function $\mathrm{sinc}(x)$ denotes $\frac{\sin(x)}{x}$. Equation (2.17) is already suitable for studying $\left|\boldsymbol{\Omega}^{\Sigma}(f)\right|$ when $f \to 0$ and $f \to \infty$.

Firstly, let's propose $\left|\boldsymbol{\Omega}^{\Sigma}(f)\right|$ and $\left|\boldsymbol{\Omega}^{s}_{j(k)}(f)\right|$ in (2.17) to be displacement spectra ($|\boldsymbol{u}^{\Sigma}(f)|$ resp. $|\boldsymbol{u}^{s}_{j(k)}(f)|$). All subevents have same scalar seismic moment M^{s}_{o}, low-frequency part of displacement spectra is proportional to M^{s}_{o}, hence low-frequency average of these spectra will be surely proportional to M^{s}_{o} and approximately equal to average subevent amplitude displacement spectra $|\boldsymbol{u}^{s}(f \to 0)|$, then

$$\lim_{f\to 0} E_{\mathcal{S}}\left\{\overline{\boldsymbol{u}^{s}_{j}(f)}\boldsymbol{u}^{s}_{j}(f)\right\} = \left|\boldsymbol{u}^{s}(f \to 0)\right|^{2} \tag{2.18}$$

$$\lim_{f\to 0} E_{\mathcal{S}}\left\{\overline{\boldsymbol{u}^{s}_{k}(f)}\boldsymbol{u}^{s}_{j}(f)\right\} = \left|\boldsymbol{u}^{s}(f \to 0)\right|^{2} \tag{2.19}$$

For $f \to 0$, using (2.17), (2.18), (2.19) and $\lim_{x\to 0}\mathrm{sinc}(x) = 1$, the square of an average amplitude displacement spectra is

$$\left|\boldsymbol{u}^{\Sigma}(f \to 0)\right|^{2} = \sum_{j=1}^{N}\left|\boldsymbol{u}^{s}(f \to 0)\right|^{2} + \sum_{\substack{j,k=1\\ j\neq k}}^{N}\left|\boldsymbol{u}^{s}(f \to 0)\right|^{2} \tag{2.20}$$

rearranging terms yields

$$\left|\boldsymbol{u}^{\Sigma}(f \to 0)\right| = \sqrt{N + N(N-1)}\left|\boldsymbol{u}^{s}(f \to 0)\right| \tag{2.21}$$

and finally

$$\left|\boldsymbol{u}^{\Sigma}(f \to 0)\right| = N\ \left|\boldsymbol{u}^{s}(f \to 0)\right| \tag{2.22}$$

Secondly, let's propose $\left|\boldsymbol{\Omega}^{\Sigma}(f)\right|$ and $\left|\boldsymbol{\Omega}^{s}_{j(k)}(f)\right|$ in (2.17) to be acceleration spectra ($|\ddot{\boldsymbol{u}}^{\Sigma}(f)|$ resp. $|\ddot{\boldsymbol{u}}^{s}_{j(k)}(f)|$). All subevents have same scalar seismic moment M^{s}_{o} and same proportions, thus same corner frequencies f^{s}_{c}. High-frequency part of acceleration spectra is proportional to $M^{s}_{o}\left(f^{s}_{c}\right)^{2}$, hence high-frequency average of these spectra will be surely proportional to $M^{s}_{o}\left(f^{s}_{c}\right)^{2}$ and approximately equal to average subevent amplitude acceleration spectra $|\ddot{\boldsymbol{u}}^{s}(f \to \infty)|$, then

$$\lim_{f\to \infty} E_{\mathcal{S}}\left\{\overline{\ddot{\boldsymbol{u}}^{s}_{j}(f)}\ddot{\boldsymbol{u}}^{s}_{j}(f)\right\} = \left|\ddot{\boldsymbol{u}}^{s}(f \to \infty)\right|^{2} \tag{2.23}$$

$$\lim_{f\to \infty} E_{\mathcal{S}}\left\{\overline{\ddot{\boldsymbol{u}}^{s}_{k}(f)}\ddot{\boldsymbol{u}}^{s}_{j}(f)\right\} = \left|\ddot{\boldsymbol{u}}^{s}(f \to \infty)\right|^{2} \tag{2.24}$$

For $f \to \infty$, using (2.17), (2.23), (2.24) and $\lim_{x\to\infty}\mathrm{sinc}(x) = 0$, the square of an average amplitude displacement spectra is

$$\left|\ddot{\boldsymbol{u}}^{\Sigma}(f \to \infty)\right|^{2} = \sum_{j=1}^{N}\left|\ddot{\boldsymbol{u}}^{s}(f \to \infty)\right|^{2} \tag{2.25}$$

and finally

$$\left|\ddot{\boldsymbol{u}}^{\Sigma}\left(f\rightarrow\infty\right)\right|=\sqrt{N}\,\left|\ddot{\boldsymbol{u}}^{s}\left(f\rightarrow\infty\right)\right| \tag{2.26}$$

From (2.22) and (2.26) it is clear that low-frequency and high-frequency parts of subevents spectra are summing up in different ways. In literature (2.22) and (2.25) has been often distinguished as coherent and incoherent summation. Coherent summation means that composite amplitude spectrum, composed of N subevents, is sum of N subevents' amplitude spectra and incoherent summation means that square of composite amplitude spectrum, composed of N subevents, is sum of N squares of subevents' amplitude spectra. Adopting terms coherent/incoherent, one can see that coherency and incoherency is proved only for limits $f\rightarrow 0$ and $f\rightarrow\infty$ respectively. To look at the composite spectrum between these two limits, we dare to assume

$$E_{\mathcal{S}}\left\{\overline{\boldsymbol{\Omega}_{j}^{s}\left(f\right)}\boldsymbol{\Omega}_{k}^{s}\left(f\right)\right\}\approx E_{\mathcal{S}}\left\{\overline{\boldsymbol{\Omega}_{j}^{s}\left(f\right)}\boldsymbol{\Omega}_{j}^{s}\left(f\right)\right\}\approx\left|\boldsymbol{\Omega}^{s}\left(f\right)\right|^{2} \tag{2.27}$$

where $\left|\boldsymbol{\Omega}^{s}\left(f\right)\right|$ denotes average subevent amplitude spectra, so (2.17) becomes

$$\left|\boldsymbol{\Omega}^{\Sigma}\left(f\right)\right|^{2}=\left|\boldsymbol{\Omega}^{s}\left(f\right)\right|^{2}\left[N+\left(N-1\right)\operatorname{sinc}^{2}\left(\frac{f\,T}{2}\right)\right] \tag{2.28}$$

Average composite displacement spectrum $\left|\boldsymbol{u}^{\Sigma}\left(f\right)\right|$ computed from (2.28) is plotted in Figure 2.1, for four different N. We can see that low-frequency levels are underestimated. Explanation is obvious. From (2.22) and (2.3) we have

$$\left|\boldsymbol{u}^{\Sigma}\left(f\rightarrow 0\right)\right|=N\,\left|\boldsymbol{u}^{s}\left(f\rightarrow 0\right)\right|\propto N\,M_{o}^{s} \tag{2.29}$$

however for $\left|\boldsymbol{u}^{m}\left(f\rightarrow 0\right)\right|$ we have from (2.3) and (2.7)

$$\left|\boldsymbol{u}^{m}\left(f\rightarrow 0\right)\right|\propto N^{\frac{3}{2}}\,M_{o}^{s} \tag{2.30}$$

so that

$$\frac{\left|\boldsymbol{u}^{m}\left(f\rightarrow 0\right)\right|}{\left|\boldsymbol{u}^{\Sigma}\left(f\rightarrow 0\right)\right|}=\sqrt{N}\;\Rightarrow\;\lim_{f\rightarrow 0}\frac{\left|\boldsymbol{\Omega}^{m}\left(f\right)\right|}{\left|\boldsymbol{\Omega}^{\Sigma}\left(f\right)\right|}=\sqrt{N} \tag{2.31}$$

On the other hand, we can see that high-frequency levels are fitted well. Explanation is also obvious. By combining (2.1) with (2.7) we get

$$\frac{f_{c}^{s}}{f_{c}^{m}}=\sqrt{N} \tag{2.32}$$

Putting (2.5) into (2.26), using (2.32), we obtain

$$\left|\ddot{\boldsymbol{u}}^{\Sigma}\left(f\rightarrow\infty\right)\right|=\sqrt{N}\,\left|\ddot{\boldsymbol{u}}^{s}\left(f\rightarrow\infty\right)\right|\propto\sqrt{N}\,M_{o}^{s}\,\left(f_{c}^{s}\right)^{2}=N^{\frac{3}{2}}\,M_{o}^{s}\,\left(f_{c}^{m}\right)^{2} \tag{2.33}$$

and for $\left|\ddot{\boldsymbol{u}}^{m}\left(f\rightarrow\infty\right)\right|$ we have from (2.5) and (2.7)

$$\left|\ddot{\boldsymbol{u}}^{m}\left(f\rightarrow\infty\right)\right|\propto M_{o}^{m}\,\left(f_{c}^{m}\right)^{2}=N^{\frac{3}{2}}\,M_{o}^{s}\,\left(f_{c}^{m}\right)^{2} \tag{2.34}$$

so that

$$\frac{\left|\ddot{\boldsymbol{u}}^{m}\left(f\rightarrow\infty\right)\right|}{\left|\ddot{\boldsymbol{u}}^{\Sigma}\left(f\rightarrow\infty\right)\right|}=1\;\Rightarrow\;\lim_{f\rightarrow\infty}\frac{\left|\boldsymbol{\Omega}^{m}\left(f\right)\right|}{\left|\boldsymbol{\Omega}^{\Sigma}\left(f\right)\right|}=1 \tag{2.35}$$

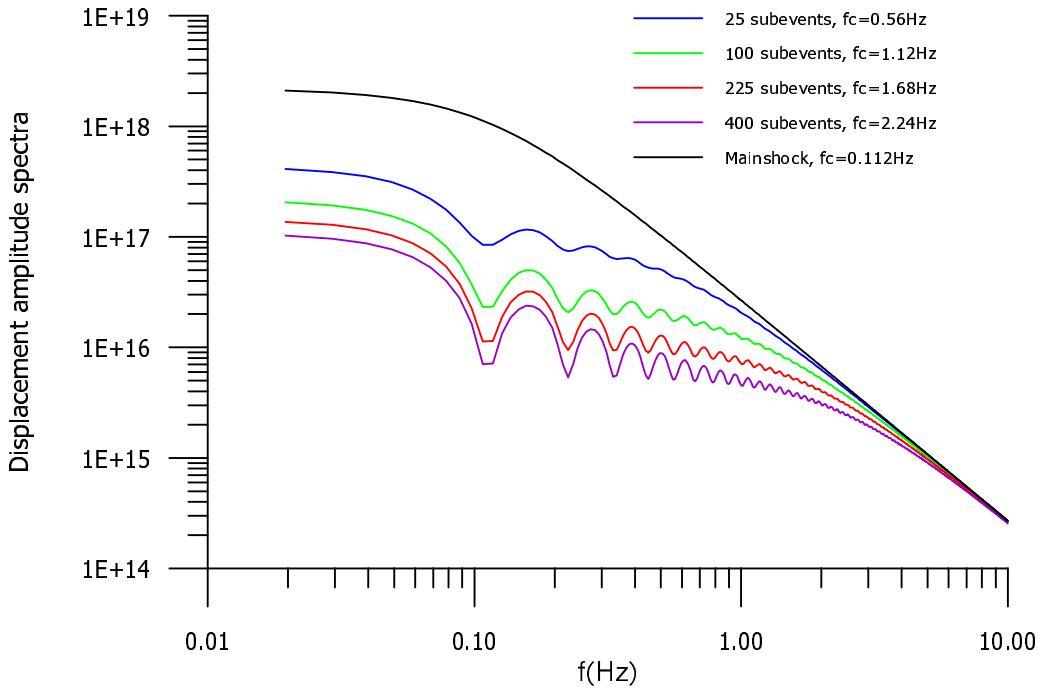

Figure 2.1: Four displacement amplitude spectra $\left|\boldsymbol{u}^{\Sigma}(f)\right|$ for different N, computed using (2.28), and the requested displacement amplitude spectrum of the mainshock $|\boldsymbol{u}^{m}(f)|$, computed using (2.2). The spectra are normalized at $f = 0$ to M_o. Corner frequencies satisfy (2.1).

2.3.2 Summation process for deterministic t_m^r

Although deterministic timing of subevents represents quite different task from random timing, we will show that it gives similar results. Let's take a radial rupture as an example case of deterministic timing of subevents. By radial rupture we mean

$$t_m^r = \frac{|\boldsymbol{\xi_m}|}{v_r} \tag{2.36}$$

where v_r is rupture velocity, $\boldsymbol{\xi_m}$ is vector pointing from hypocenter of the mainshock to the nucleation point of the m-th subevent, which is usually taken in the center of m-th subfault. For further discussion, it is useful to denominate frequencies f, $f \in (0, f_c^m)$ low frequencies, $f \in (f_c^m, f_c^s)$ middle frequencies and $f \in (f_c^s, \infty)$ high frequencies. Let's generally propose that low-frequency contributions sum coherently, high-frequency contributions incoherently and middle-frequency contributions partly coherently. Although we have no mathematical proof for such proposition (rate of coherency/incoherency is strongly dependent on the total number of subevents N and on given value of rupture velocity v_r), we will provide qualitative explanation. To explain coherency at low frequencies, we can follow an example of kinematic models of finite source. In kinematic modelling of faulting one has to provide coherent summation over whole desired frequency band. In other words, fault elements have to be small enough, such that time differences between arrivals from adjacent elements are less then periods of interests. Six elements on the shortest wavelength is usually considered to be sufficient to provide correct summation (see section 4.1 for description in more detail). Back to composite modelling, it is reasonable to assume that the number of subevents along dip and strike is same, thus equal to $\sqrt{N}$. Then we can imagine that we have $\sqrt{N}$ elements on wavelength equal to length L^m of the mainfault, which is inversely proportional to f_c^m. Because $\sqrt{N}$ is usually greater then 5, we are convinced that coherent summation is provided for frequencies bellow f_m^c. We emphasize that elements in kinematic modelling don't have same meaning as subevents in composite modelling, but the criteria of coherent summation can be handled for both cases in the same way. On the other hand, high-frequency ($f > f_c^s$) contributions sum incoherently. Explanation is obvious. Time differences between rupture times of two adjacent subevents are greater than periods of interest, thus t_m^r appears to be random variable from high-frequency point of view (time shifts are too big to catch rapid changes of subevent contribution). Hence we can apply results for high frequencies, derived in previous section (see section 2.3.1). Figure 2.2 show schematically example of both coherent and incoherent summation. Figure 2.2 can be interpreted in two different ways: 1) $T_a = T_b$, $t_a = \frac{1}{4}t_b \Rightarrow$ showing influence of different timing; 2) proposing self-similar function plotted at two different time scales, so that $T_a = 4T_b$, $t_a = t_b \Rightarrow$ showing the fact, that lower frequency contributions are summed coherently and higher frequency contributions are summed incoherently.

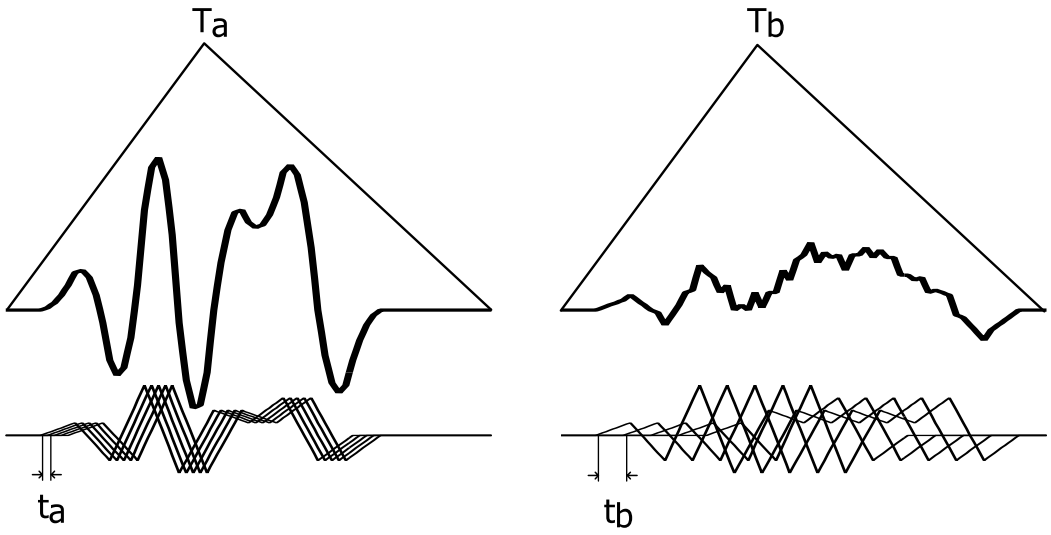

Figure 2.2: Coherent versus incoherent summation at two time windows of length T_a resp. T_b, with time differences t_a resp. t_b. Bold line represents sum of thin lines, which are bellow the bold line.

To summarize results of this section, we declare that low-frequency contributions of subevents sum coherently producing underestimated low-frequency part of composite spectra (see (2.31)). The high-frequency contributions of subevents sum incoherently, producing requested level of composite spectra (see (2.35)). Middle frequencies are mix of both coherent and incoherent energy. Accurate rate of coherency/incoherency in middle frequencies depends mostly on total number of subevents. The higher number of subevents we have, the more coherent summation is above the corner frequency of the mainshock. Other parameters may play role too (rupture velocity, changes of impulse response of medium over the mainfault).

2.4 Correction at low frequencies

Results of previous section show that summation made by applying (2.8) produces correct level of high-frequency part of the composite spectra, but also produces wrong level of low-frequency part. This problem was resolved by number of authors in various ways (Joyner and Boore (1986), Boatwright (1988), Irikura and Kamae (1994), Frankel (1995), Beresnev and Atkinson (1997)). We have chosen the method presented by Frankel (1995), because it seems to be the simplest one and it also includes reasonable physical explanation. Correct spectral level at low frequencies is obtained by simple linear filtering of composite spectra computed

from (2.8). Filtering function is constructed taking into account (2.31) and (2.35), so that frequencies bellow corner frequency of the mainshock have to be boosted $\sqrt{N}$-times and frequencies above corner frequency of the subevent should remain unchanged. At middle frequencies we don't have any special constraint about the filter's amplitude spectrum, it should only smoothly decay from value $\sqrt{N}$ to value 1. An example of such amplitude spectrum is

$$|S(f)| = C\frac{1+\left(\frac{f}{f_c^s}\right)^{\varepsilon}}{1+\left(\frac{f}{f_c^m}\right)^{\varepsilon}} \tag{2.37}$$

where f_c^s is corner frequency of the subevent, f_c^m is corner frequency of the mainshock,ε is parameter determining shape and C is constant determined from conditions

$$|S(f \to 0)| = \sqrt{N} \tag{2.38}$$
$$|S(f \to \infty)| = 1 \tag{2.39}$$

so combining (2.37) with (2.38) and (2.39), we get

$$\lim_{f\to 0} C\frac{1+\left(\frac{f}{f_c^s}\right)^{\varepsilon}}{1+\left(\frac{f}{f_c^m}\right)^{\varepsilon}} = C \quad \Rightarrow \quad C = \sqrt{N} \tag{2.40}$$

$$\lim_{f\to \infty} C\frac{1+\left(\frac{f}{f_c^s}\right)^{\varepsilon}}{1+\left(\frac{f}{f_c^m}\right)^{\varepsilon}} = C\left(\frac{f_c^m}{f_c^s}\right)^{\varepsilon} \quad \Rightarrow \quad C\left(\frac{f_c^m}{f_c^s}\right)^{\varepsilon} = 1 \tag{2.41}$$

Since C is determined from (2.40), (2.41) becomes

$$\left(\frac{f_c^s}{f_c^m}\right)^{\varepsilon} = \sqrt{N} \tag{2.42}$$

It is clear that ε should be 1 to preserve consistency with (2.32). However, plotting (2.37) for $\varepsilon = 1$ produces amplitude spectra, which decays immediately at frequencies lower than f_c^m (see Figure 2.3). Hence, boosting low frequency part of spectrum, especially at frequencies near f_c^m, is insufficient. To solve this problem, we substitute f_c^m by formal corner frequency f_c^x. Then (2.42) becomes

$$f_c^x = \frac{f_c^s}{\sqrt[2\varepsilon]{N}} \tag{2.43}$$

Now putting $\varepsilon = 2$ or $\varepsilon = 3$ produces $f_c^x \neq f_c^m$, particularly $f_c^x > f_c^m$. Formal parameter f_c^x controls the range of frequencies which are exactly amplified $\sqrt{N}$-times, that is why we use it instead of f_c^m in (2.37) (see Figure 2.3). Particularly, we choose $\varepsilon = 2$, so f_c^x would not differ much from f_c^m, but low-frequency

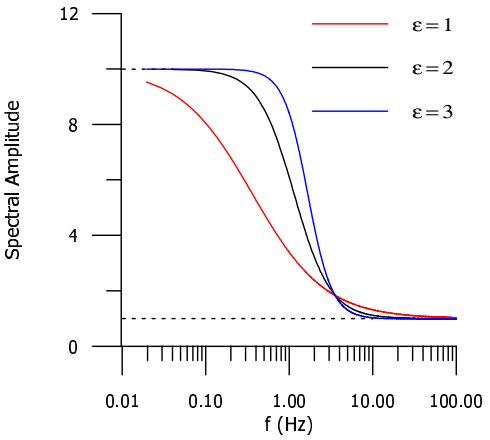

Figure 2.3: Amplitude spectra of filtering function computed from (2.37) substituting f_c^m by f_c^x for N=100, $f_c^s = 3.56$, $f_c^m = 0.36$. f_c^x is known from (2.43) for different ε: $\varepsilon = 1 \Rightarrow f_c^x = f_c^m$ (red); $\varepsilon = 2 \Rightarrow f_c^x = 1.13$ (black); $\varepsilon = 3 \Rightarrow f_c^x = 1.65$ (blue)

contributions would be boosted sufficiently. The case of $\varepsilon = 2$ is also preferred by Frankel (1995) and Hartzell et al. (1999). Amplitude spectra of the required filter is then

$$|S(f)| = \sqrt{N} \frac{1 + \left(\frac{f}{f_c^s}\right)^2}{1 + \left(\frac{f}{f_c^x}\right)^2} \tag{2.44}$$

where

$$f_c^x = \frac{f_c^s}{\sqrt[4]{N}} \tag{2.45}$$

A causal operator with amplitude spectrum given by (2.44) is found using equivalence

$$x(t) \quad \text{is causal} \quad \Leftrightarrow \quad \Im[X(f)] = \mathfrak{H}\{\Re[X(f)]\} \tag{2.46}$$

where $X(f)$ is Fourier transform of $x(t)$, $\Im$ and $\Re$ denotes imaginary resp. real part of an complex number, symbol $\mathfrak{H}\{\ldots\}$ is used for Hilbert transform. We can write

$$S(f) = |S(f)| \; e^{i\,\phi(f)} \tag{2.47}$$

where $|S(f)|$ is the amplitude spectrum of $S(f)$ and $\phi(f)$ is the unknown phase spectrum of $S(f)$. Applying on (2.47) logarithm, we get

$$\log S(f) = \log |S(f)| + i\,\phi(f) \tag{2.48}$$

Let's assume $\log S(f)$ to be spectrum of causal function, then by applying equivalence (2.46) we obtain

$$\phi(f) = \mathfrak{H}\{\log |S(f)|\} \tag{2.49}$$

so that

$$S(f) = |S(f)| \; e^{i\,\mathfrak{H}\{\log|S(f)|\}} \tag{2.50}$$

The result is complex spectrum of requested filtering function (see Figure 2.4, in

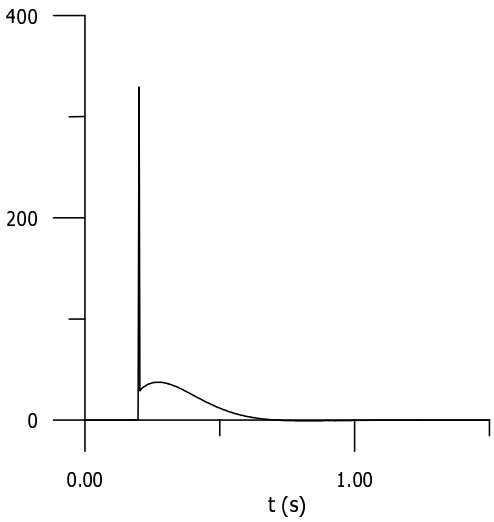

Figure 2.4: Filtering function in time domain, computed applying inverse Fourier transform on (2.50) (signal was shifted to better resolve delta function at the beginning). N=100, $f_c^s = 3.56$, $f_c^m = 0.36$, $f_c^x = 1.13$

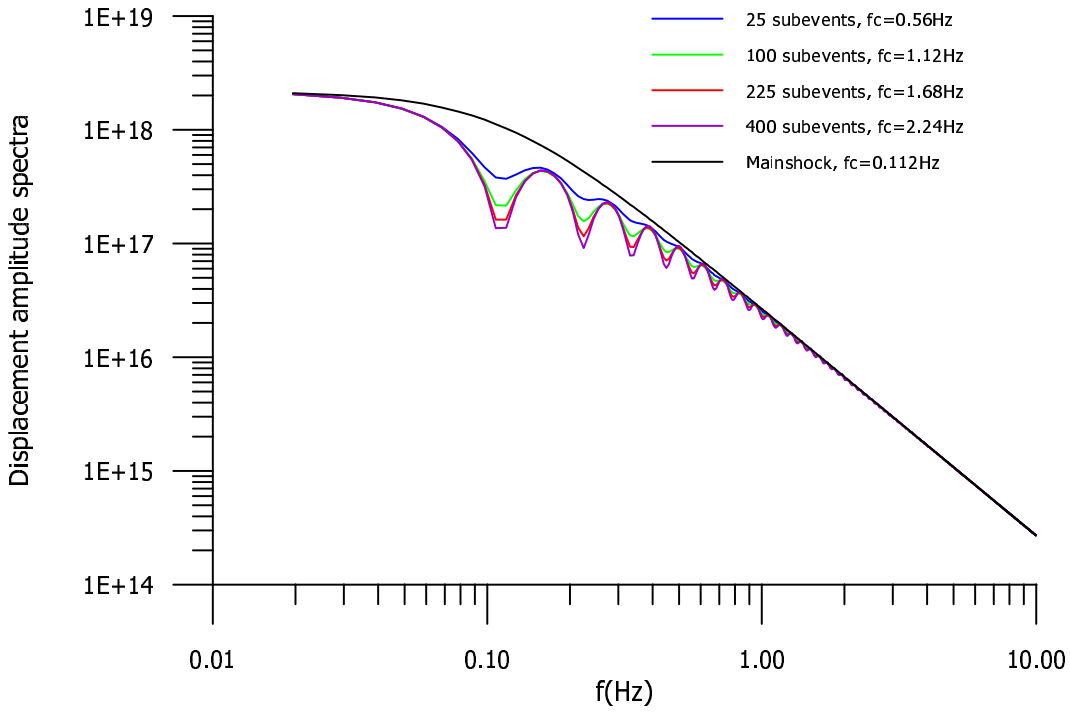

Figure 2.5: Four displacement amplitude spectra $\left|\boldsymbol{u}^{\Sigma}(f)\right|$ for different N, computed from (2.28) and multiplied by (2.44), with the requested displacement amplitude spectrum of the mainshock $|\boldsymbol{u}^{m}(f)|$, computed using (2.2). The spectra are normalized at $f = 0$ to M_o. Corner frequencies satisfy (2.1).

time domain). Incorporating linear filter $S(f)$ into our summation method (2.8), we get

$$\mathbf{\Omega}^{\Sigma}(t) = s(t) * \sum_{m=1}^{N} \mathbf{\Omega}_m^s (t - t_m^r) \tag{2.51}$$

where $s(t)$ is inverse Fourier transform of $S(f)$ and asterisk $*$ denotes convolution. Figure 2.1 was recomputed using filtering function. The result is in Figure 2.5. We can see, that both very low and very high frequencies spectral levels are correct, however middle frequencies spectral levels are slightly underestimated.

Physical basis of such filtering is that low frequencies of the mainshock are controlled by long-wavelength variations of slip over the mainfault. Subevents obviously don't contain such information about these long-wavelength variations, thus one has to enhance them (for example by linear filtering). For detailed explanation see Frankel (1995), Frankel (1991) and Boatwright (1988).

2.5 Synthetic test

Algorithm of the summation provided above assure proper scaling of both low and high frequency parts of composite spectra. However, scaling of middle frequency spectral levels was not resolved properly, because of the complexity of the summation process at these frequencies (frequencies between corner frequency of the mainshock and corner frequency of the subevent). Irikura and Kamae (1994) showed, that for high number of subevents ($N \gtrsim 400$) there are significant sags from ω^{-2} spectrum. Tumarkin and Archuleta (1994) were solving similar problem of spectral deficiencies close to corner frequency of the mainshock. On the other hand, Frankel (1995) didn't mention any problems with the shape of modelled spectra at middle frequencies. With respect to these uncertain propositions, we decided to perform simple synthetic test to study behavior of our composite model, especially at middle frequencies. Time histories of subevents for this test were obtained using stochastic approach, similar to one presented by Boore (1983). Particularly, we generated Gaussian white noise and next we multiplied it by shape of ω^{-2} amplitude acceleration spectra (see relation (2.4)). Summation was provided using (2.51) and (2.36). Resulting spectra was identified with spectra of acceleration time history at some virtual station. The source parameters of the modelled mainshock (see Table 2.1) were set to common values for event of magnitude $M_w = 6.2$ (see Somerville et al. (1999)). Test was performed for set of different N (total number of subevents). 100 realizations of subevents' time histories was generated for each value of N. The result of the test is shown in Figure 2.6. Curves labelled

M_o^m	$2.16\ 10^{18} Nm$
L^m	$25000\,m$
W^m	$25000\,m$
$\langle v_r \rangle$	$2800\,m\,s^{-1}$
f_c^m	$0.11\,Hz$

Table 2.1: Source parameters of modelled event.

as synthetic amplitude spectra represents average modelled spectra (average is made over 100 generated time histories of subevents).

We can see, that modelled spectra show significant discrepancies with requested shape of spectra, similar to ones shown by Irikura and Kamae (1994). To avoid such discrepancies from ω^{-2} source model, we were forced to look for more sophisticated composite model. The idea of non-equal sized subevents, improving middle frequencies, comes from Irikura and Kamae (1994) and we expand it in next chapter.

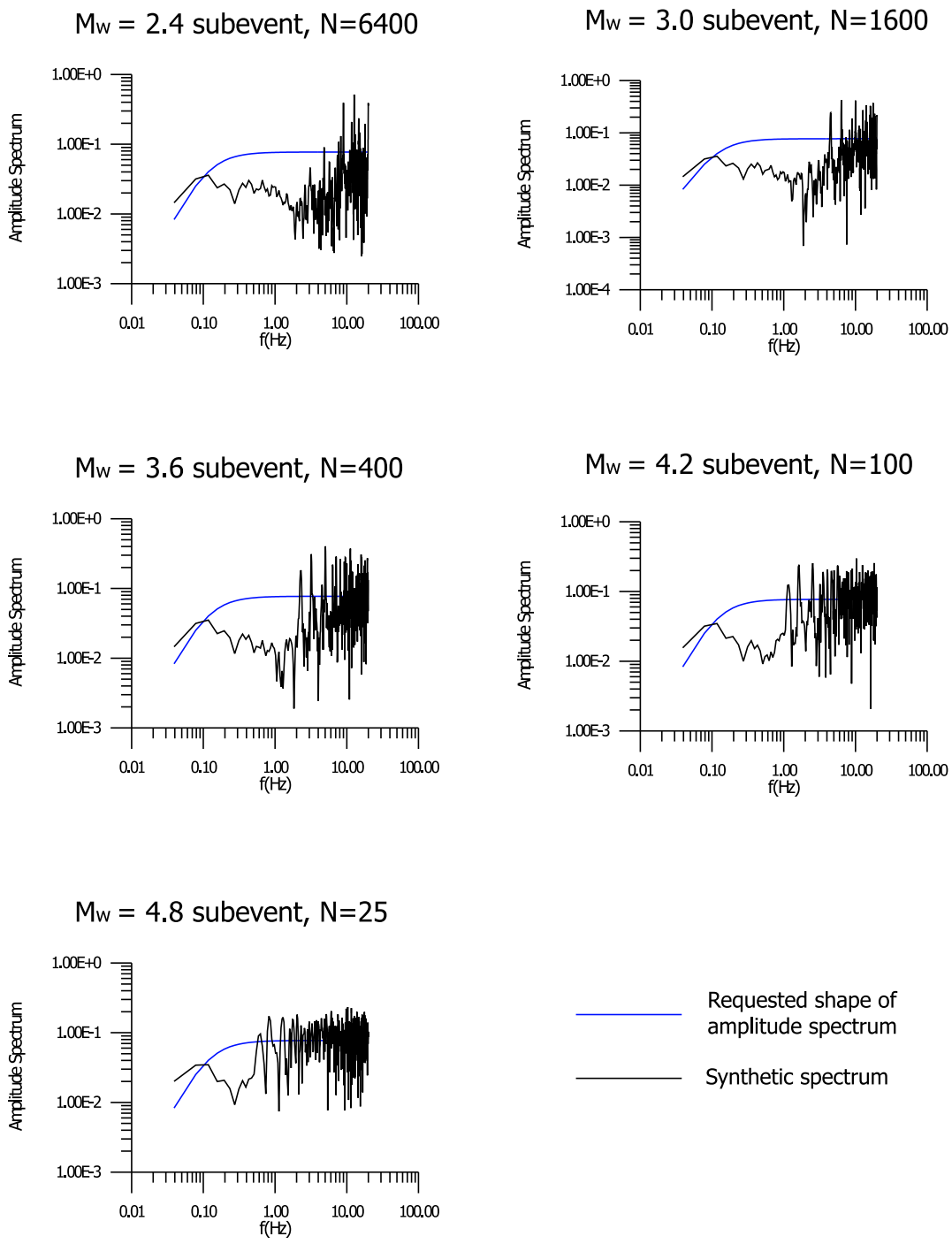

Figure 2.6: Modelling $M_w = 6.2$, using tapered white noise as a time history of subevent. The subevent moment magnitude ranges from 2.4 to 4.8.

Chapter 3

Subevents with non-equal sizes

Concept of non-equal sized subevents was firstly proposed by Boatwright (1982). Further, Frankel (1991) expanded and generalized that idea to the statistical source model with a continuous, self-similar distribution of subevent sizes, finding relations, which controls the high-frequency behavior of composite spectra with respect to scaling of stress drop and particular size distribution of subevents. We adopted that model and making some improvements tried to use it in practice. Several successful applications of such models (Irikura and Kamae (1994), Zeng et al. (1994), Zeng and Anderson (1996), Hartzell et al. (1999)) gave us motivation for this part of study.

3.1 Fractal subevent size distribution

As we proposed above, our adopted model is self-similar. It means, that the way how behavior of level $i+1$ subevents affects level i subevent is same for all levels (see Figure 3.1). This allows us to solve only the problem of mainshock and level 1 subevents. In next lines, we are going to determine high-frequency falloff of the mainshock, evaluating the total high-frequency energy of level 1 subevents. Derivation is made following Frankel (1991), providing some modifications. We notice, that we will strictly hold the total area of level 1 subevents equal to the area of the mainshock, because this is, from our point of view, the only natural condition for the total area of level 1 subevents. However, other authors (see Zeng et al. (1994), Zeng and Anderson (1996)) used successfully the total area of level 1 subevents greater than area of the mainshock.

Self-similar distributions can be quantified using fractal concept (see Turcotte (1989)). So that the number N of subevents with characteristic dimension greater than or equal to R, occurring within mainshock area ($\propto R_{main}^2$), can be treated as

$$N(R) \propto \left(\frac{R_{main}}{R}\right)^D \tag{3.1}$$

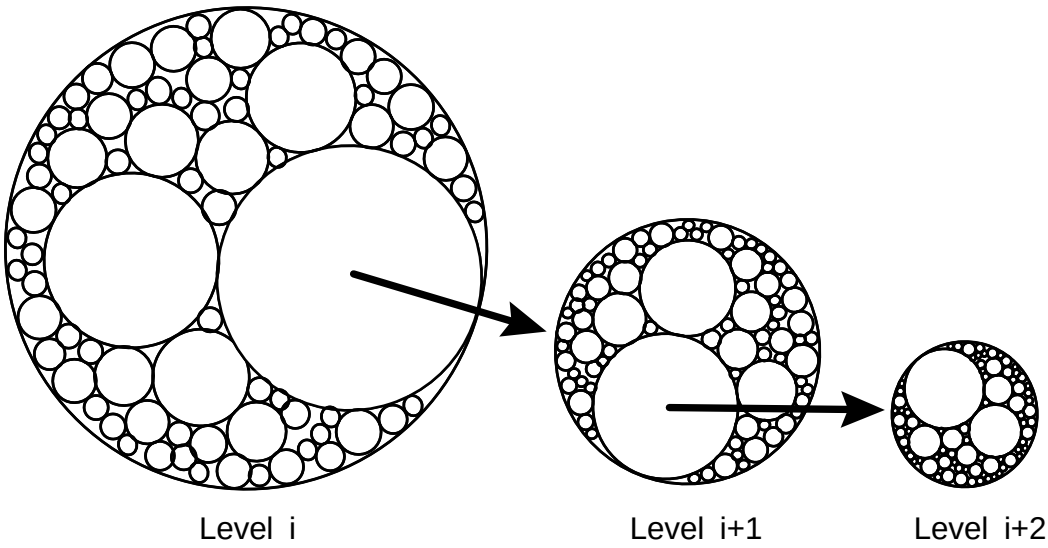

Figure 3.1: Self-similar composite model

where D is fractal dimension. The corresponding probability density function is

$$\frac{dN\left(R\right)}{dR} \propto \frac{R_{main}^{D}}{R^{D+1}} \tag{3.2}$$

Further, we assume that displacement spectral amplitude $\Omega\left(f\right)$ of subevent source function decays as a power γ of frequency above corner frequency f_c:

$$\Omega\left(f\right) \propto \frac{M_o}{1+\left(\frac{f}{f_c}\right)^{\gamma}} \tag{3.3}$$

where M_o is the seismic moment of the subevent. The amplitude spectrum of radiated energy is proportional to the square of the velocity spectral amplitude, so

$$E\left(f\right) \propto f^2\Omega^2\left(f\right) \tag{3.4}$$

For high frequencies ($f >> f_c$), relation (3.3) reduce to

$$\Omega\left(f\right) \propto f^{-\gamma} f_c^{\gamma} M_o \tag{3.5}$$

so for high frequencies we can write (3.4) in way

$$E\left(f\right) \propto f^{2-2\gamma} f_c^{2\gamma} M_o^2 \tag{3.6}$$

For seismic moment we have relation

$$M_o \propto \Delta u\left(R\right) R^2 \tag{3.7}$$

where Δu is final slip, which is treated as a linear function of R. Final slip Δu can be associated with a static stress drop $\Delta\sigma$, which represents the difference between stress on the subevent before and after rupture, using relation

$$\Delta\sigma \propto \frac{\Delta u\,(R)}{R} \tag{3.8}$$

so we can write

$$M_o \propto \Delta\sigma R^3 \tag{3.9}$$

However, static stress drop can be generally dependent on the subevent's size R. We prescribe dependence in form

$$\Delta\sigma \propto R^{\eta} \tag{3.10}$$

By combining (3.10) and (3.9) with (3.6) we get

$$E\,(f) \propto f^{2-2\gamma} f_c^{2\gamma} R^{2\eta+6} \tag{3.11}$$

Since corner frequency f_c is inversely proportional to subevent size R, (3.11) becomes

$$E\,(f) \propto f^{2-2\gamma} R^{2\eta-2\gamma+6} \tag{3.12}$$

Total high-frequency energy $dE(f)$ radiated by subevents with sizes within the range $(R, R+dR)$ can be expressed as

$$dE\,(f) \propto E\,(f)\; dN \tag{3.13}$$

where dN is number of subevents with size within a range $(R, R+dR)$. Then using (3.2) we get

$$dE\,(f) \propto f^{2-2\gamma} R^{2\eta-2\gamma-D+5} R_{main}^{D}\, dR \tag{3.14}$$

where dE is total high-frequency energy radiated by subevents with sizes within the range $(R, R+dR)$. Further we introduce R_{min} and R_{max} which denote minimal and maximal size of level 1 subevents within mainshock, respectively. The high-frequency content of subevents sums incoherently (see sections 2.3.2 and 2.3.1), so that their energy is additive. By "high-frequency" we mean frequencies $f >> f_{c,min}$, where $f_{c,min}$ is the corner frequency of the smallest subevent[1]. Therefore the energy of the mainshock E_{main} at a given frequency f ($f >> f_{c,min}$) can be determined evaluating integral

$$E_{main}\,(f) \propto \int_{R_{min}}^{R_{max}} \frac{dE\,(f)}{dR}\, dR \tag{3.15}$$

[1]denotation $f_{c,min}$ may be misleading; although it is linked with the smallest subevent (as shown by the subscript), it represents the highest denoted frequency in the model.

Since E_{main} must satisfy (3.12) for $R = R_{main}$, we obtain

$$f^{2-2\gamma} R_{main}^{2\eta-2\gamma+6} = p \int_{R_{min}}^{R_{max}} f^{2-2\gamma} R^{2\eta-2\gamma-D+5} R_{main}^{D}\, dR \tag{3.16}$$

where p is constant of proportionality. Obvious modifications of (3.16) will produce

$$R_{main}^{2\eta-2\gamma-D+6} = p \int_{R_{min}}^{R_{max}} R^{2\eta-2\gamma-D+5}\, dR \tag{3.17}$$

Now it's possible to eliminate p, by assuming that the sum of subevents' areas is equal to the area of the mainshock. For simplicity, we assume circular subevents. The area $A_{sub}(R)$ of the subevent with radius R is

$$A_{sub}(R) = \pi R^2 \tag{3.18}$$

The total area dA of the subevents with radii within $(R, R + dR)$ is given by

$$dA(R) = \pi p R^{-D+1} R_{main}^{D} dR \tag{3.19}$$

and finally the total area A of all subevents is

$$A = p\pi R_{main}^{D} \int_{R_{min}}^{R_{max}} R^{-D+1}\, dR \tag{3.20}$$

Assuming A equal to he area of the mainshock πR_{main}^2, (3.20) becomes

$$\frac{1}{p} = R_{main}^{D-2} \int_{R_{min}}^{R_{max}} R^{-D+1}\, dR \tag{3.21}$$

The integral (3.21) has two different solutions according to parameter D. Since now, our derivation slightly differs from the one, presented by Frankel (1991). In case of $D = 2$, we get

$$\frac{1}{p} = [\ln R]_{R_{min}}^{R_{max}} \tag{3.22}$$

and in case of $D \neq 2$, we get

$$\frac{1}{p} = R_{main}^{D-2} \left[\frac{R^{-D+2}}{-D+2} \right]_{R_{min}}^{R_{max}} \tag{3.23}$$

Substituting (3.22) and (3.23) into (3.17) produces

$$D = 2\,, \qquad R_{main}^{2\eta-2\gamma+4} = \frac{1}{\ln \frac{R_{max}}{R_{min}}} \int_{R_{min}}^{R_{max}} R^{2\eta-2\gamma+3}\, dR \tag{3.24}$$

$$D \neq 2\,, \qquad R_{main}^{2\eta-2\gamma+4} = \frac{2-D}{R_{max}^{2-D} - R_{min}^{2-D}} \int_{R_{min}}^{R_{max}} R^{2\eta-2\gamma-D+5}\, dR \tag{3.25}$$

One can easily prove that

$$\frac{1}{\ln \frac{R_{max}}{R_{min}}} \int_{R_{min}}^{R_{max}} R^{-1}\, dR = 1 \tag{3.26}$$

$$\frac{2-D}{R_{max}^{2-D} - R_{min}^{2-D}} \int_{R_{min}}^{R_{max}} R^{1-D}\, dR = 1 \tag{3.27}$$

hence variables γ, η have to satisfy relation

$$\eta - \gamma + 2 = 0 \tag{3.28}$$

for all values of D. Rearranging terms in (3.28), we get the final expression for high-frequency falloff γ

$$\gamma = \eta + 2 \tag{3.29}$$

It means that high-frequency $f >> f_{c,min}$ spectral falloff γ depends only on scaling stress drop with subevent's radius, described by η, and is independent of the fractal dimension D. The relation (3.29) differs from that one derived by Frankel (1991),

$$\gamma = \eta - \frac{D}{2} + 3 \tag{3.30}$$

That is caused by preserving the condition, that the sum of subevents' areas is in our derivation equal to the area of the mainshock for all values of D.

It is useful to evaluate shape of composite spectra, to verify results derived above and to study their behavior for frequencies between the corner frequency of the mainshock and the corner frequency of the smallest subevent (often called middle-frequencies). Presuming for a while incoherent summation even in the middle-frequencies, a composite spectral amplitude $\Omega^{\Sigma}(f)$ at given frequency f can be expressed as

$$\Omega^{\Sigma}(f) = \sqrt{\int_{R_{min}}^{R_{max}} \left(\Omega_{\gamma}(f,R)\right)^2 \frac{dN}{dR}\, dR} \tag{3.31}$$

where $\Omega_{\gamma}(f,R)$ is contribution of subevents with size R, high-frequency slope γ to the composite spectrum at given frequency f. All terms have to be expressed by variable R and parameters γ and D, using suitable relations derived above in this chapter. The results for $R_{min} = 1\,km$, $R_{max} = 5\,km$, $R_{main} = 10\,km$ and for number of different sets of parameters are shown in Figure 3.2. For high-frequencies $f >> f_{c,min}$ both composite spectra match the falloff γ, the high-frequency falloff of the subevents (self-similarity is preserved) and the mainshock. The high-frequency fall-off, described by γ, seem to be really independent of D. For the middle-frequencies $f_{c,min} > f > f_{c,main}$ the composite spectrum becomes slowly insufficient, because the summation process in the middle frequencies becomes partially coherent, however we assumed incoherent summation. One could expect

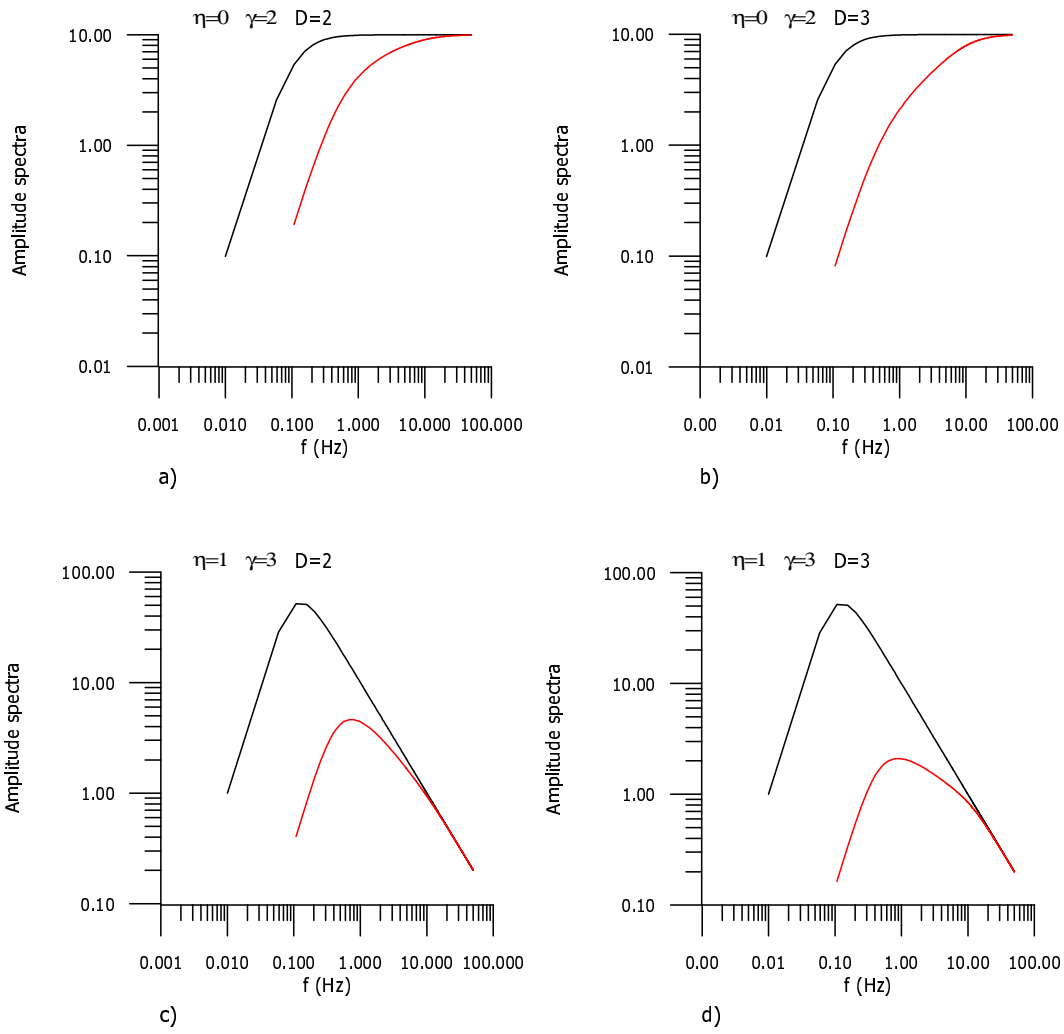

Figure 3.2: Requested amplitude acceleration spectra of the mainshock (black) and composite amplitude acceleration spectra (red) for four sets of parameters. Parameters were chosen to verify (3.31), especially the independence γ of D.

better results for the middle-frequencies, if we sum up time series directly, taking into account partial coherency.

Further, Frankel (1991) showed independently[2], that D and η are related in way

$$D = 2 - \eta \tag{3.32}$$

Substituting η in (3.29) by D, using (3.32), we get

$$\gamma = 4 - D \tag{3.33}$$

while Frankel (1991) obtained (using (3.30))

$$\gamma = 5 - \frac{3}{2}D \tag{3.34}$$

The expressions (3.33) and (3.34) can be directly compared, one can see that they become same for $D = 2$.

In further study we prefer $\eta = 0$, $\gamma = 2$, $D = 2$. As we proposed above (see (3.32), (3.33)), just one of these η, γ, D can be treated independently. Thus the choice $D = 2$, $\eta = 0$, $\gamma = 2$ can be explained in three different ways. We can hold $D = 2$ (produces $\eta = 0$, $\gamma = 2$), as well as we can hold $\gamma = 2$ (produces $D = 2$, $\eta = 0$), as well as we can hold $\eta = 0$ (produces $D = 2$, $\gamma = 2$). All of these three values seem to be acceptable independently and it's appreciable that they fully satisfy equations (3.32), (3.33). The choice $D = 2$, $\eta = 0$, $\gamma = 2$ is supported by number of papers. Hanks (1979) and Andrews (1980) have suggested that stress drop independent of seismic moment ($\eta = 0$) produces ω^{-2} high-frequency spectral falloff. Bernard (1996) successfully applied $D = 2$ in modelling stochastic slip distribution. Moreover, Mai and Beroza (2001) analyzed recent source inversions for number of great earthquakes, getting fractal dimension $D = 2.3$ of final slip distribution, Somerville et al. (1999) indicates $D \backsimeq 2$, too.

[2]here without proof

3.2 Discrete realization of FSSD

To use the fractal subevent size distribution (for short, FSSD) in practice, one has to evolute its discretized form. Following Irikura and Kamae (1994), we are going to produce discrete distribution of subevents, which meets the probability density function, here denoted $n(R)$, (3.2) for $D = 2$

$$n(R) = \begin{cases} 0 & 0 < R < R_{min} \\ \frac{dN(R)}{dR} = p\frac{R_{main}^2}{R^3} & R_{min} < R < R_{max} \\ 0 & R_{max} < R < R_{main} \end{cases} \tag{3.35}$$

We propose finite integer number M of subevent types. The type of subevent is defined by its size R_i $(i = 1, \ldots, M)$. Subevent with size R_i is going to represent subevents with size within a range $(R_i, R_i + \Delta R)$. In other words, number N_i of subevents with size R_i is equal to number of subevents with size within the range $(R_i, R_i + \Delta R)$, so

$$N_i = n(R_i)\,\Delta R \tag{3.36}$$

For all R_i within (R_{min}, R_{max}) we have

$$N_i = p\frac{R_{main}^2}{R_i^3}\Delta R \tag{3.37}$$

In practice, the fault is usually taken as a rectangle. That's why we assume rectangular subevents and further, for simplicity, square subevents. The constant of proportionality p will be determined by letting the sum of subevents' areas equal to the mainshock area:

$$\sum_{i=1}^{M} N_i R_i^2 = R_{main}^2 \tag{3.38}$$

then putting (3.37) into (3.38) produces

$$p = \frac{1}{\sum_{i=1}^{M} \frac{\Delta R}{R_i}} \tag{3.39}$$

thus (3.37) becomes

$$N_i = \frac{R_{main}^2}{\sum_{j=1}^{M} \frac{\Delta R}{R_j}} \frac{\Delta R}{R_i^3} \tag{3.40}$$

The choice of ΔR is not trivial, although it may look like. If we simply set ΔR as

$$\Delta R = \frac{R_{max} - R_{min}}{M} \tag{3.41}$$

we obtain common equidistant subdivision of the range (R_{min}, R_{max}). (3.40) then produces N_i efficiently equal to zero for higher R_i. In other words, we

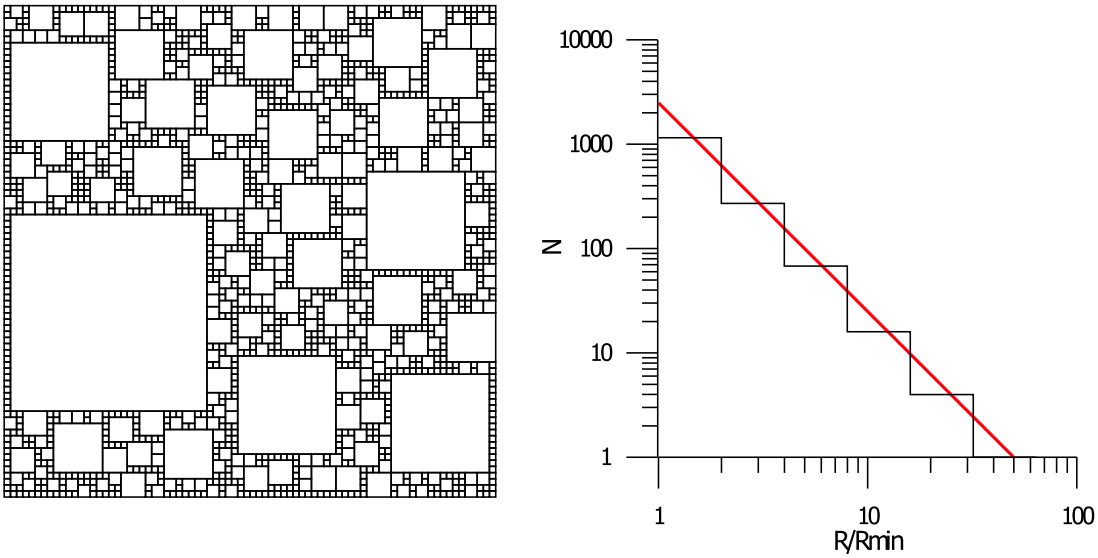

Figure 3.3: Discrete realization of FSSD with following parameters: $M = 6$, $R_{main} = 80\,R_{min}$, $R_{max} = 64\,R_{min}$. Histogram on right side show appropriate distribution of numbers of subevents with respect to their sizes. Red line denotes R^{-2} decay.

get efficiently non-zero values of N_i only for smallest types of subevents. For example, we will consequently fill the mainfault only with two types of subevents, however we prescribed $M = 6$ (M becomes efficiently equal to two, although it was formally set to 6, because $N_i \doteq 0$ for $i > 2$). It is clear, that the higher number of subevents types in the model is, the better representation of continuous subevent size distribution is achieved. So we request the high numbers M of subevents' types to be exactly present in the model ($N_i \geq 1$, for all $i = 1 \ldots M$). We solved the problem by setting

$$\Delta R = \Delta R_i \tag{3.42}$$

then

$$R_{i+1} = R_i + \Delta R_i \tag{3.43}$$

It is clear that ΔR_i has to increase with increasing R_i to get the number N_M of greatest subevents equal minimally to one. Particularly, we put

$$\Delta R_i = c^{i-1}\,\Delta R_1 \tag{3.44}$$

where c is constant greater then 1 and ΔR_1 is width of first interval, represented by subevent with size R_{min}. The choice of c and ΔR_1 is not arbitrary, because condition

$$\sum_{i=1}^{M} \Delta R_i = R_{max} - R_{min} \tag{3.45}$$

has to be satisfied. By substituting (3.44) into (3.45), we obtain

$$\Delta R_1 \sum_{i=1}^{M} c^{i-1} = R_{max} - R_{min} \tag{3.46}$$

and using relation for sum of geometric progression with quotient c, we get

$$\Delta R_1 = \frac{c-1}{c^{M-1}-1} \left(R_{max} - R_{min}\right) \tag{3.47}$$

The value of ΔR_1 is thus determined by choice of c. Hence, the number of subevents N_i with size equal to R_i is

$$N_i = \frac{R_{main}^2}{\sum_{j=1}^{M} \frac{\Delta R_j}{R_j}} \frac{\Delta R_i}{R_i^3} \tag{3.48}$$

where $\Delta R_{i(j)}$ is determined from

$$\Delta R_i = c^{i-1} \frac{c-1}{c^{M-1}-1} \left(R_{max} - R_{min}\right) \tag{3.49}$$

The optimal value of parameter c was found $c \cong 2$. Now if N_i are generated properly, it is not problem to distribute the subevents randomly (we incorporate stochastic component to the source modelling) over the mainfault, so they don't overlap with each other. In Figure 3.3, we can see an example of one realization of FSSD generated by subroutine FRACTAL. A hardcopy of the subroutine with brief description is placed in Appendix. To preclude any confusions about R_{max}, we suggest that R_{max} denotes $R_M + \Delta R_M$. As it was proposed above, subevents within the range $(R_M, R_M + \Delta R_M)$ are represented by subevent with size R_M. Hence, the biggest subevent visible in Figure 3.3 has size R_M (particularly $R_M = 32\, R_{min}$), not R_{max} (particularly $R_{max} = 64\, R_{min}$).

3.3 Summation process for FSSD

In this section we will construct summation scheme in similar way as it was done for equal sized subevents in Chapter 2. At the end of section 3.1 we have proposed that we prefer constant stress drop scaling (in 3.1 represented by $\eta = 0$) and ω^{-2} source model (in 3.1 represented by $\gamma = 2$). Hence, we can incorporate into our considerations sections 2.1, 2.2, so we can use results of Chapter 2, just adjusting them to be consistent with FSSD. We propose

$$\mathbf{\Omega}^{\Sigma}(t) = \sum_{j=1}^{M} s_j(t) * \sum_{i=1}^{N_j} \mathbf{\Omega}_i^j \left(t - t_{ij}^r\right) \tag{3.50}$$

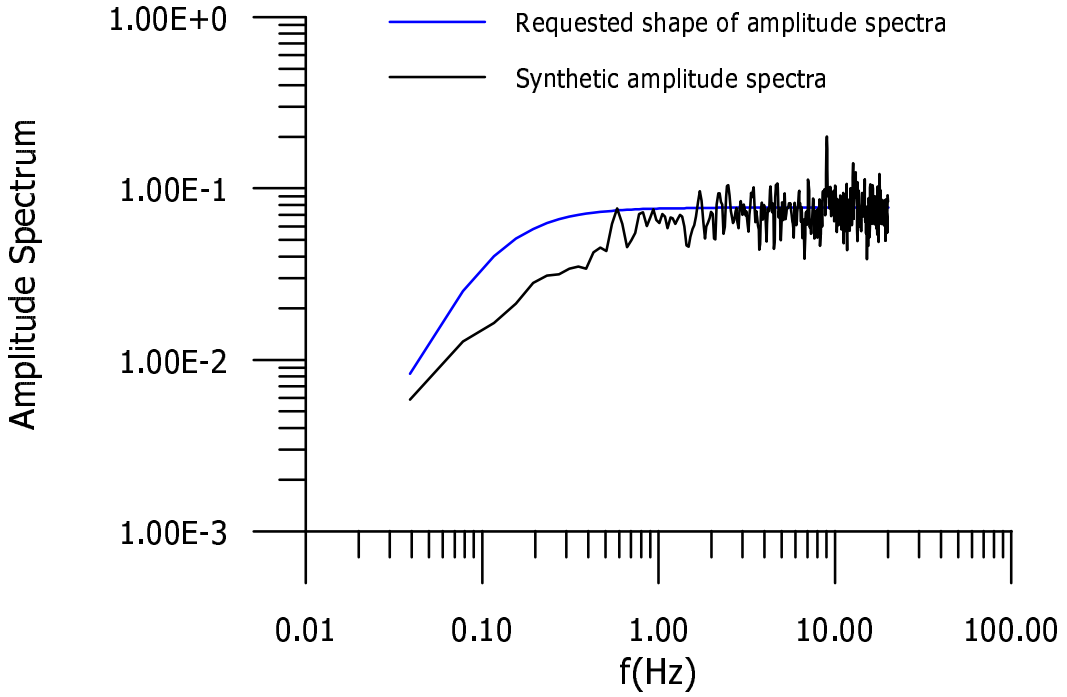

Figure 3.4: Modelling $M_w = 6.2$, using tapered white noise as a time history of subevent for one realization of FSSD with following parameters: $M = 6$; $R_{min} = 312.5m$ $R_{main} = 80\,R_{min}$; $R_{max} = 64\,R_{min}$ (the distribution depicted in Figure 3.3). The subevent moment magnitude ranges from 2.4 to 5.4.

where $\mathbf{\Omega}^{\Sigma}(t)$ is modelled composite time history, M denotes number of subevents types, subscript j denote subevent type, $s_j(t)$ is filtering function similar to the one introduced in section 2.4, N_j denotes number of j-th type subevents. $\mathbf{\Omega}_i^j\left(t - t_{ij}^r\right)$ is time history of ij-th subevent (i-th subevent of j-th type), t_{ij}^r is time when ij-th subevent is initialized. N_j is determined from (3.48) for given values of M, R_{main}, R_{min} and R_{max} (see section 3.2 for detailed description). To obtain amplitude spectra of filtering functions s_j, we cannot use directly (2.44), because N is not defined in model with non-equal sized subevents. We override this formal problem by putting (2.7) into both (2.44) and (2.45), so

$$|S(f)| = \left(\frac{M_o^m}{M_o^j}\right)^{\frac{1}{3}} \frac{1 + \left(\frac{f}{f_c^j}\right)^2}{1 + \left(\frac{f}{f_c^x}\right)^2} \tag{3.51}$$

$$f_c^x = f_c^j \left(\frac{M_o^j}{M_o^m}\right)^{\frac{1}{6}} \tag{3.52}$$

where M_o^j, f_c^j are scalar seismic moment and corner frequency of j-th subevent type respectively. Next we show, that summation scheme described above pro-

duces correct levels of composite amplitude spectra. We assume that low-frequency contributions sum coherently (see sections 2.3.1 and 2.3.2), thus using (2.1) and (2.3) produces

$$\begin{aligned}\left|\boldsymbol{u}^{\boldsymbol{\Sigma}}\left(f\to 0\right)\right| &= \sum_{j=1}^{M}\left|s_j\left(f\to 0\right)\right|\sum_{i=1}^{N_j}\left|\boldsymbol{u}_{\boldsymbol{i}}^{\boldsymbol{j}}\left(f\to 0\right)\right| \propto \sum_{j=1}^{M}\left(\frac{M_o^m}{M_o^j}\right)^{\frac{1}{3}}\sum_{i=1}^{N_j}M_o^j = \\ &= \sum_{j=1}^{M}\left(\frac{M_o^m}{M_o^j}\right)^{\frac{1}{3}} N_j\, M_o^j = \sum_{j=1}^{M}\left(\frac{M_o^m}{M_o^j}\right)^{\frac{1}{3}} \frac{R_{main}^2}{\sum_{k=1}^{M}\frac{\Delta R_k}{R_k}}\,\frac{\Delta R_j}{R_j^3}\,M_o^j = \\ &= \frac{1}{\sum_{k=1}^{M}\frac{\Delta R_k}{R_k}}\sum_{j=1}^{M}\left(\frac{M_o^m}{M_o^j}\right)^{\frac{1}{3}}\left(\frac{M_o^m}{M_o^j}\right)^{\frac{2}{3}}\frac{\Delta R_j}{R_j}\,M_o^j = M_o^m \end{aligned} \tag{3.53}$$

so low frequency levels of composite spectra are scaled properly. High-frequency contributions, we assume, sum incoherently (see sections 2.3.1 and 2.3.2), thus using (2.1) and (2.5) produces

$$\begin{aligned}\left|\ddot{\boldsymbol{u}}^{\boldsymbol{\Sigma}}\left(f\to\infty\right)\right|^2 &= \sum_{j=1}^{M}\left|s_j\left(f\to\infty\right)\right|^2\sum_{i=1}^{N_j}\left|\ddot{\boldsymbol{u}}_{\boldsymbol{i}}^{\boldsymbol{j}}\left(f\to\infty\right)\right|^2 \propto \\ &\propto \sum_{j=1}^{M}\sum_{i=1}^{N_j}\left(M_o^j\,\left(f_c^j\right)^2\right)^2 = \sum_{j=1}^{M} N_j\left(M_o^j\right)^2\left(f_c^j\right)^4 = \\ &= \frac{1}{\sum_{k=1}^{M}\frac{\Delta R_k}{R_k}}\sum_{j=1}^{M}\frac{\Delta R_j}{R_j}\frac{R_{main}^2}{R_j^2}\left(M_o^j\right)^2\left(f_c^j\right)^4 = \\ &= \frac{1}{\sum_{k=1}^{M}\frac{\Delta R_k}{R_k}}\sum_{j=1}^{M}\frac{\Delta R_j}{R_j}\left(\frac{M_o^m}{M_o^j}\right)^{\frac{2}{3}}\left(M_o^j\right)^2\left(\frac{M_o^m}{M_o^j}\right)^{\frac{4}{3}}\left(f_c^m\right)^4 = \\ &= \frac{1}{\sum_{k=1}^{M}\frac{\Delta R_k}{R_k}}\sum_{j=1}^{M}\frac{\Delta R_j}{R_j}\left(M_o^m\right)^2\left(f_c^m\right)^4 = \left(M_o^m\,\left(f_c^m\right)^2\right)^2 \end{aligned} \tag{3.54}$$

so high frequency levels of composite spectra are scaled properly.

We recomputed synthetic test described in the section 2.5 (see section 2.5 for detailed description of the test), applying FSSD and summation scheme represented by (3.50). The result is in Figure 3.4. Curve labelled as a synthetic amplitude spectra represents an average modelled spectrum (average is made over 100 generated time histories of subevents) for one realization of FSSD. We can see that discrepancies in middle frequencies spectral levels were successfully removed. But on the other hand, we obtain slight underestimation of low frequencies ($f < 0.6Hz$). However, strong motion seismology is focused on higher frequencies, where is our model correct.

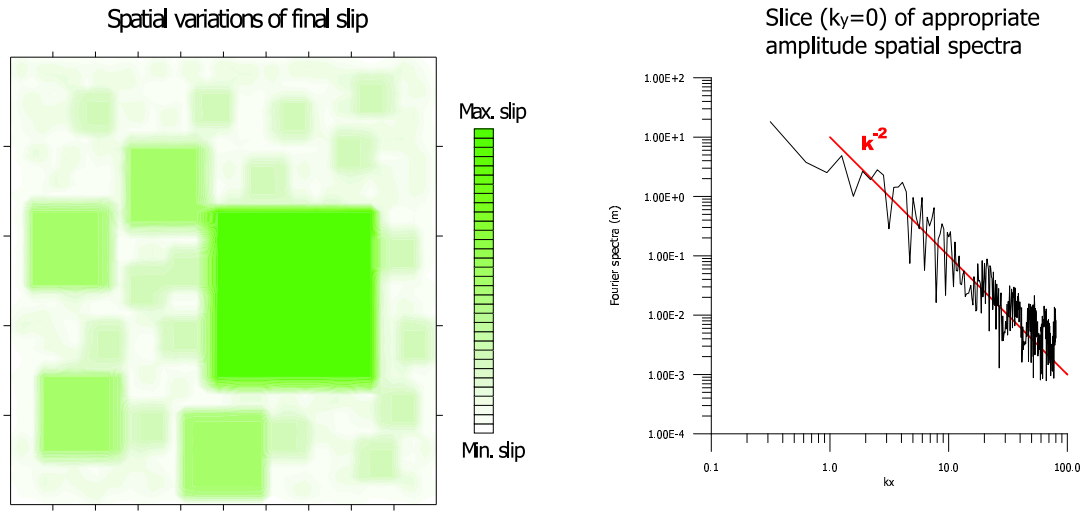

Figure 3.5: Final slip spatial variations for one realization of FSSD with following parameters: $M = 6$, $R_{main} = 80\,R_{min}$, $R_{max} = 64\,R_{min}$. The graph on the right side shows the slice ($k_y = 0$) of appropriate 2D amplitude spatial spectrum. Red line denotes k^{-2} decay.

3.4 Spatial variations of final slip

Looking carefully at (2.1), one can see that non-equal sized subevent distributed over the mainfault produce spatial variations of final slip over the mainfault. Particularly

$$\langle u \rangle^j = \left(\frac{M_o^j}{M_o^m} \right)^{\frac{1}{3}} \langle u \rangle^m \tag{3.55}$$

where $\langle u \rangle^j$ and $\langle u \rangle^m$ denote average final slip of j-th subevent type and mainshock respectively. But taking into account (3.51) and (3.52), it becomes clear that low frequency contributions are boosted exactly to one level, same for all subevent types. This level is proportional to $\langle u \rangle^m$. Thus we get homogenous slip at low frequencies. On the other hand, filtering functions don't affect high frequencies. Hence we obtain spatial variations of final slip (see Figure 3.5) only at high frequencies. We analyzed these spatial variations by 2D Fourier transform, getting k^{-2} decay of slice ($k_y = 0$) of 2D amplitude spatial spectrum (see Figure 3.5). The k^{-2} slip distribution is proposed by theoretical studies Bernard et al. (1996), Hisada (2000), Hisada (2001) and it also seems to be verified by analyzes of recent seismic source inversions (see Mai and Beroza (2001), Somerville et al. (1999)). That is why we believe, that our model is well constrained.

Chapter 4

Modelling of subevents

Time histories of subevents can be generally obtained by several ways. Most common is to use aftershocks as time histories of subevents (Irikura and Kamae (1994), Frankel (1995), Hartzell et al. (1999)), which is usually called EGF method (Empirical Green's Function method). Although EGF method carries advantage of full information on source-receiver propagation effects, it has limited range of applicability (regions without seismic stations, signal/noise ratio, determination of aftershock's mechanism, etc.). Thus it is inconvenient for prediction of strong ground motion. Other approach is using synthetic time histories of subevents. These can be obtained using either deterministic methods (finite-difference methods, discrete wave number method, etc.) applied by Zeng et al. (1994), Zeng and Anderson (1996), Hartzell et al. (1999) or stochastic methods, where the synthetics are obtained by filtering of white noise, applied with particular modifications by Beresnev and Atkinson (1998), Kamae et al. (1998), Hartzell et al. (1999). We decided to follow fully deterministic approach of subevents' modelling.

4.1 Kinematic modelling of subevents

Using representation theorem (Aki and Richards, 1980), the ground displacement $\boldsymbol{U}(\boldsymbol{x},t)$ at position $\boldsymbol{x}$ and time t is

$$U_k(\boldsymbol{x},t) = \int_\Sigma m_{pq}(\boldsymbol{\xi},t) * \frac{\partial G_{kp}(\boldsymbol{x},\boldsymbol{\xi},t-t^r(\boldsymbol{\xi}))}{\partial \xi_q}\, d\Sigma \tag{4.1}$$

where Σ denotes rupture fault of subevent, m_{pq} is component of surface seismic moment density tensor, $\boldsymbol{\xi}$ determines position on the subfault, G_{kp} is a component of Green's tensor and t^r is rupture time. The asterisk $*$ denotes convolution. Just for pure shear

$$m_{pq}(\boldsymbol{\xi},t) = \mu\, \Delta u(\boldsymbol{\xi})\, s(\boldsymbol{\xi},t)\ (n_p\, \nu_q + n_q\, \nu_p) \tag{4.2}$$

where μ is shear modul, $\Delta u\left(\boldsymbol{\xi}\right)$ is final slip, $s\left(\boldsymbol{\xi},t\right)$ is slip function, $\boldsymbol{n}$ and $\boldsymbol{\nu}$ are vectors determined by focal mechanism (for detailed description see Aki and Richards, 1980)). Rewriting (4.1), using (4.2) and properties of convolution

$$U_k\left(\boldsymbol{x},t\right)=\int_{\Sigma}\mu\,\Delta u\left(\boldsymbol{\xi}\right)s\left(\boldsymbol{\xi},t-t^r\left(\boldsymbol{\xi}\right)\right)\left(n_p\,\nu_q+n_q\,\nu_p\right)*\frac{\partial G_{kp}\left(\boldsymbol{x},\boldsymbol{\xi},t\right)}{\partial\xi_q}\,d\Sigma \tag{4.3}$$

By discretizing (4.3) we get

$$U_k\left(\boldsymbol{x},t\right)=\sum_{i=1}^{n_L}\sum_{j=1}^{n_W}\mu\,\Delta u_{ij}\,s_{ij}\left(t-t^r_{ij}\right)\left(n_p\,\nu_q+n_q\,\nu_p\right)*\left.\frac{\partial G_{kp}\left(\boldsymbol{x},\boldsymbol{\xi},t\right)}{\partial\xi_q}\right|_{\boldsymbol{\xi}_{ij}}\Delta\Sigma \tag{4.4}$$

where n_L and n_W are numbers of discrete elements along strike and dip, $\Delta\Sigma$ is area of element, Δu_{ij}, t^r_{ij} and $s_{ij}\left(t\right)$ are final slip, rupture time and slip function on ij-th element, respectively and $\boldsymbol{\xi}_{ij}$ determines center of ij-th element. Now, we rewrite (4.4) in terms, which are suitable for our procedure

$$\boldsymbol{U}\left(\boldsymbol{x},t\right)=\sum_{i=1}^{n_L}\sum_{j=1}^{n_W}\mu\,\Delta u_{ij}\,s_{ij}\left(t-t^r_{ij}\right)*\tilde{\boldsymbol{G}}_{ij}\left(\boldsymbol{x},t\right)\,\Delta\Sigma \tag{4.5}$$

$$\tilde{\boldsymbol{G}}_{ij}\left(\boldsymbol{x},t\right)=\left(n_p\,\nu_q+n_q\,\nu_p\right)\left.\frac{\partial G_{kp}\left(\boldsymbol{x},\boldsymbol{\xi},t\right)}{\partial\xi_q}\right|_{\boldsymbol{\xi}_{ij}}\boldsymbol{e}_k \tag{4.6}$$

where $\boldsymbol{e}_k$ is set of base vectors in which we exactly compute ground displacement $\boldsymbol{U}\left(\boldsymbol{x},t\right)$, $\tilde{\boldsymbol{G}}_{ij}\left(\boldsymbol{x},t\right)$ can be directly computed in 1-D medium by DW-code (Bouchon (1981), Coutant (1989)) and we will call it impulse response. The technical details of computation of impulse responses are discussed in section 4.3. It is very reasonable to provide summation process in frequency domain, hence we transform (4.5) in

$$\boldsymbol{U}\left(\boldsymbol{x},f\right)=\sum_{i=1}^{n_L}\sum_{j=1}^{n_W}\mu\,\Delta u_{ij}\,s_{ij}\left(f\right)\exp\left(-2\pi\,f\,t^r_{ij}\right)\,\tilde{\boldsymbol{G}}_{ij}\left(\boldsymbol{x},f\right)\,\Delta\Sigma \tag{4.7}$$

In next sections, we are going to discus each parameter in more detail.

4.1.1 Final slip and slip velocity function on the subevent

As it is written above, we use kinematic approach for modelling subevents - relatively small earthquakes compared to the mainshock. That's why we presume to make Δu_{ij} and $s_{ij}\left(f\right)$ independent of their position on the fault (we get subscripts ij off). Final slip $\overline{\Delta u}$ of the subevent is related to its characteristic dimension using (2.1). As slip velocity function $\dot{s}(t)$ we favor functions which have ω^{-1} decay in frequency domain (e.g. box-car), because we need ω^{-2} decay in displacement spectra (as in standard Haskell model, see Lay and Wallace (1995)), on each subevent.

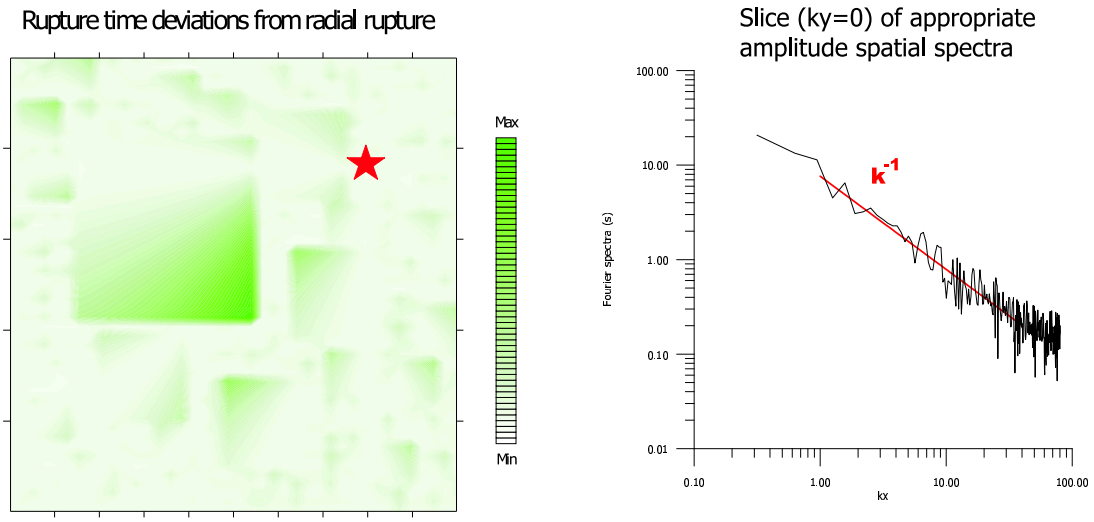

Figure 4.1: Spatial distribution of rupture times deviations from radial rupture, for one realization of FSSD with following parameters: $M = 6$, $R_{main} = 80\,R_{min}$, $R_{max} = 64\,R_{min}$. The red star denotes the hypocenter of the mainshock. The graph on the right side shows the slice ($k_y = 0$) of appropriate 2D amplitude spatial spectrum. Red line denotes k^{-1} decay.

4.1.2 Rupture time

In our case we assume the rupture front spreads radially from nucleation point with constant rupture velocity v_r. As a nucleation point can be taken generally any point of the subevent. Rupture time t^r_{ij} is exactly the time between nucleation of subevent and the moment, when the rupture front meets the center of ij-th element of the subevent. Thus for t^r_{ij} we have

$$t^r_{ij} = \frac{\sqrt{(i\,\Delta L - \xi^0_1)^2 + (j\,\Delta W - \xi^0_2)^2}}{v_r} \tag{4.8}$$

where ΔL and ΔW are length and width of element, respectively, $\boldsymbol{\xi}^0$ is a vector in the subfault determining a position of the nucleation point of the subevent. Particularly, we choose as the nucleation point of the subevent the closest point to the mainshock hypocenter. Let's have look what such choice causes in combination with radial rupture on the subevent, independent subevent timing (determined from (2.36)) and fractal subevent size distribution. To summarize the facts, the mainfault is cut into number of subevents, which are further cut into number of integrating elements, so that mainfault is in fact cut into these integrating elements, too. If we modelled the mainshock fully kinematically using radial rupture with constant v_r, we would get obviously continuous spatial distribution of timing of the integrating elements with respect to mainshock's hypocenter. However, introducing subevents with independent radial ruptures causes the deviations from

such continuous spatial distribution. Especially on the borders of the subevents, the timing of the integration elements with respect to mainshock's hypocenter becomes discontinuous. The case of one rupture velocity for both spreading rupture on subevents and for timing of subevents (used in (2.36)), is depicted in Figure 4.1. We analyzed obtained spatial distribution of these deviations from radial rupture by 2D Fourier transform, getting k^{-1} decay of slice ($k_y = 0$) of 2D amplitude spatial spectrum (see Figure 4.1). This result doesn't coincidence with theoretical propositions of Hisada (2000) and Hisada (2001). However, spatial variations of rupture velocity over the mainfault of recent earthquakes have not been studied systematically yet. We emphasize, that our proposition of inhomogeneous rupture velocity is introduced artificially and miss any deeper physical explanation, but on the other hand is not in direct contradiction with any observations.

4.1.3 Sampling of the fault plane

Sampling of the fault plane is usually expressed in form of number of samples k on minimal computed wavelength λ_{min}. The numbers n_L and n_W of samples along strike and dip are

$$n_L = \frac{L}{\frac{\lambda_{min}}{k}} \tag{4.9}$$

$$n_W = \frac{W}{\frac{\lambda_{min}}{k}} \tag{4.10}$$

where L is length and W is width of the fault. λ_{min} can be expressed by f_{max}, the highest computed frequency, using relation

$$\lambda_{min} = \frac{v_r}{f_{max}} \tag{4.11}$$

where v_r is rupture velocity, which is in our case constant. Rupture velocity is considered here instead of v_P and v_S (P-wave and S-wave velocity), because $v_P > v_S > v_r$ usually, thus λ_{min} is guaranteed to be minimal. Putting (4.11) in (4.9), (4.10), we get

$$n_L = \frac{k\, f_{max}}{v_r} L \tag{4.12}$$

$$n_W = \frac{k\, f_{max}}{v_r} W \tag{4.13}$$

The total number M of samples over fault is

$$M = n_L\, n_W = \left(\frac{k\, f_{max}}{v_r}\right)^2 L\, W \tag{4.14}$$

and f_{max} is given by

$$f_{max} = N\, \Delta f \tag{4.15}$$

where N is number of frequencies computed, Δf is step in frequency domain. The summation process is made in frequency domain, so the total number N_{TOT} of computing steps is

$$N_{TOT} = 2\,M\,N \tag{4.16}$$

The multiplication by 2 appears here because computed spectrum is a complex function (real and imaginary parts are computed separately). Using (4.14) and (4.15), we get

$$N_{TOT} = 2\,N^3 \left(\frac{k\,\Delta f}{v_r}\right)^2 L\,W \tag{4.17}$$

The above derivation is for fixed n_L, n_W independent of the calculated frequency. We attempted to decrease N_{TOT} by modifying (4.12) resp. (4.13) in the way that $n_L = n_L(f)$ resp. $n_W = n_W(f)$, particularly substituting f_{max} by f

$$n_L = \frac{k\,f}{v_r} L \tag{4.18}$$

$$n_W = \frac{k\,f}{v_r} W \tag{4.19}$$

Then the number M_j of computing steps, needed for j-th frequency $f = j\,\Delta f$, is

$$M_j = 2 \left(\frac{k\,\Delta f}{v_r}\right)^2 L\,W\,j^2 \tag{4.20}$$

and the sum over whole desired frequency band produce

$$N_{TOT} = \sum_{j=1}^{N} 2 \left(\frac{k\,\Delta f}{v_r}\right)^2 L\,W\,j^2 \tag{4.21}$$

Using relation

$$\sum_{j=1}^{N} j^2 = \frac{N\,(N+1)\,(2N+1)}{6} \tag{4.22}$$

yields

$$N_{TOT} = 2\,\frac{2N^3 + 3\,N^2 + N}{6} \left(\frac{k\,\Delta f}{v_r}\right)^2 L\,W \tag{4.23}$$

N_{TOT} is plotted in Figure 4.2 as function of N using (4.17) and (4.23). If we divide (4.17) by (4.23), then for $N \to \infty$, we get

$$\lim_{N\to\infty} \frac{6N^3}{2N^3 + 3\,N^2 + N} = 3 \tag{4.24}$$

In other words, for high N we need only one third of computing steps, compared to the case of sampling independent of frequency. By high N we mean $N > 50$, approximately (Figure 4.2).

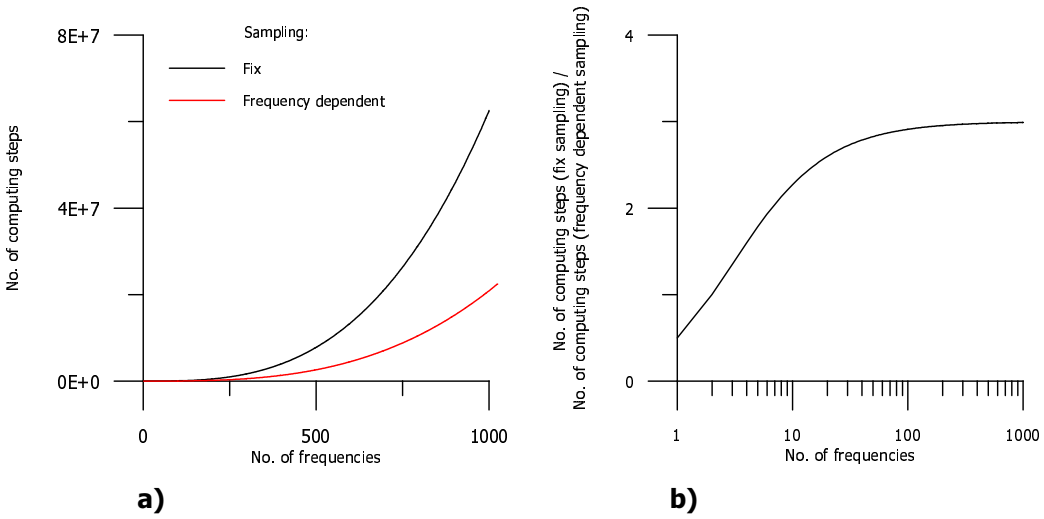

Figure 4.2: a) Number of computing steps needed when using fix sampling (black) and frequency dependent sampling (red), b) Ratio between the number of computing steps using fix and frequency dependent sampling

The choice of k depends mainly on a relative position of the receiver and the fault plane. Computed spectrum has to be independent of k. As a rule $k = 6$ is often considered, but it can be shown, that in some special cases it's not dense enough. On the other hand, in some other cases even lower value (e.g. $k = 2$) is enough. That's important, because computing time is proportional to k^2 (see (4.23)), so setting up k low can save computing time significantly.

As we proposed above, kinematic modelling is exactly numerical evaluation of integral (4.1). The summation with fixed sampling is the most primitive way of numerical integration. With frequency-dependent sampling we exactly take into account influence of integration parameter f on a final result of integration. The method of integration can be likely further improved.

4.2 Point-source approximation of subevents

Point-source approximation is an another approach to earthquake source modelling. Although it has limited extents of application, it simplifies and speeds up the computation significantly. Approximation is carried from (4.1) (see Aki and Richards (1980) for more details) getting

$$U_k(\boldsymbol{x}, t) \doteq M_{pq}(t) * \left. \frac{\partial G_{kp}(\boldsymbol{x}, \boldsymbol{\xi}, t)}{\partial \xi_q} \right|_{\boldsymbol{\xi}_o} \tag{4.25}$$

where $\boldsymbol{\xi}_o$ denotes center of the subevent, M_{pq} is seismic moment tensor determined from

$$M_{pq}(t) = \mu \, \overline{\Delta u} \, L \, W \, s(t) \, (n_p \, \nu_q + n_q \, \nu_p) \tag{4.26}$$

where $\overline{\Delta u}$ is an average slip on the subevent, L and W are length and width of the subevent. The rest of parameters appearing in (4.25) and (4.26) is described in section 4.1. Putting (4.26) into (4.25) produces

$$\boldsymbol{U}(\boldsymbol{x}, t) = \mu \, L \, W \, \overline{\Delta u} \, s(t) * \tilde{\boldsymbol{G}}_o(\boldsymbol{x}, t) \tag{4.27}$$

$$\tilde{\boldsymbol{G}}_o(\boldsymbol{x}, t) = (n_p \, \nu_q + n_q \, \nu_p) \left. \frac{\partial G_{kp}(\boldsymbol{x}, \boldsymbol{\xi}, t)}{\partial \xi_q} \right|_{\boldsymbol{\xi}_o} \boldsymbol{e}_k \tag{4.28}$$

where $\tilde{\boldsymbol{G}}_o$ is exactly the impulse response introduced in section 4.1.

Average final slip $\overline{\Delta u}$ of subevent is related to its characteristic dimension using (2.1). Spectrum of source time function $\dot{s}(t)$ (derivative of slip function $s(t)$) of the subevent is prescribed following Brune (1970):

$$\dot{s}(f) = \frac{1}{\left(1 + i \frac{f}{f_c^s}\right)^2} \tag{4.29}$$

where i is imaginary unit and f_c^s is corner frequency of subevent, which is in our case determined from

$$f_c = a \frac{v_r}{R} \tag{4.30}$$

where v_r is rupture velocity, R denotes characteristic dimension of subevent and a is free parameter constant for all subevents. The choice of a play great role in prediction of strong ground motion, because higher a causes higher f_c^s which causes the higher level of the plateau of acceleration spectrum (see (2.5)), thus it should be handled very carefully. From our practical point of view, it seems to be feasible to use $a = 1$ (see chapter 5) for subevents which are nearly squares.

4.3 Calculation of impulse responses

In case of kinematic modelling, impulse response of medium, as it was defined in section 4.1, is needed in finite number of points covering subevent. As the subevents fully fill up the mainfault we need impulse responses in grid covering the mainfault. Density of such grid depends of maximal computed frequency. In section 4.1.3 it was shown that the number of elements (points of grid) grows rapidly going into high frequencies. Thus the number of impulse response needed grows too. Although the computation of impulse response with DW-code (Bouchon (1981), Coutant (1989)) is simple and quite fast, time and memory requests become unjustifiable for such numbers of impulse responses (thousands). The frequency dependent sampling presented in section 4.1.3 accelerates the summation

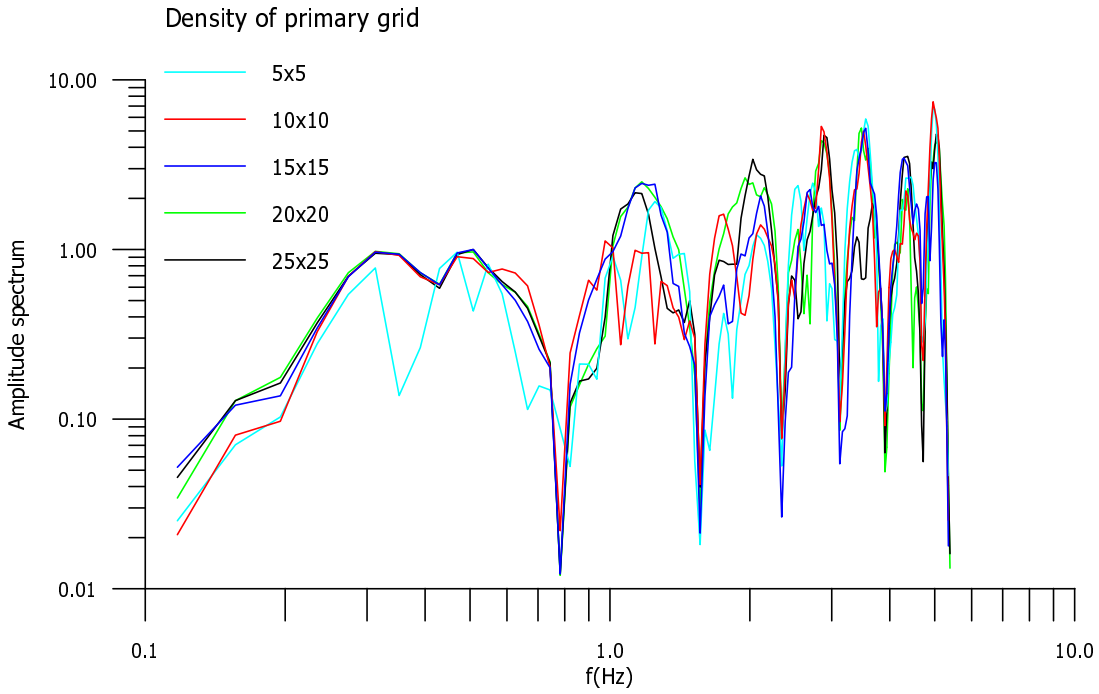

Figure 4.3: The influence of density of primary grid, on resulting spectra. Case of kinematic modelling of subevents.

itself, but it doesn't solve growing requirements on number of impulse responses. It makes the requirements even higher, because with every new sampling we need generally new set of impulse responses. To overcome these problems we introduce interpolation of impulse responses over the mainfault. Particularly, we use 2D cubic spline interpolation taken from Press et al. (1992). The outline of algorithm is obvious. At first we compute impulse responses by DW-code in fixed grid (one can call it primary grid) covering the rectangle which contains the mainfault. It is important to compute impulse responses in points which are out of the mainfault too, to perform reliable interpolation up to borders of the mainfault. The interpolation of complex spectra (real and imaginary parts are treated independently) from such a grid is made step by step for each frequency, getting spectra of impulse response in any arbitrary point of the mainfault. This allows us to use frequency dependent sampling without growing requirements on the number of impulse responses. We emphasize, that we don't say that such interpolation of impulse responses allows us to go with computations to very high frequencies, leaving the primary grid, from which is the interpolation made, untouched. We expect that spectra of the impulse responses at high frequencies would not be so smooth, to be transcribed by relatively low number of values, so to compute high frequencies we need to make interpolation from denser grid. The influence of density of primary grid on resulting composite spectra is shown

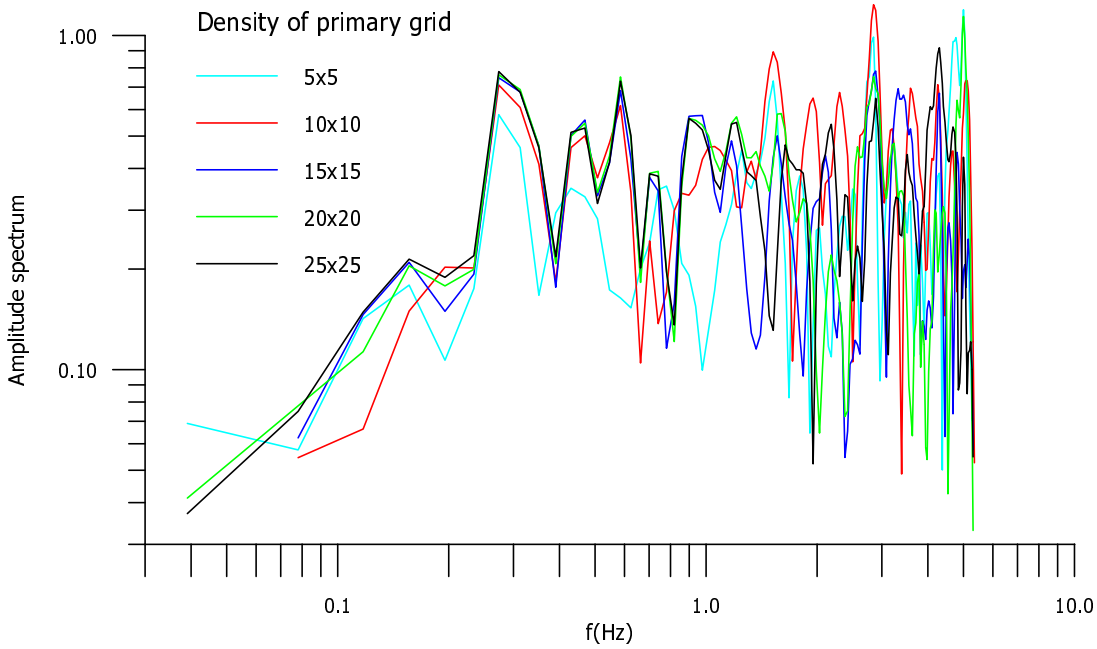

Figure 4.4: The influence of density of primary grid, on resulting spectra. Case of modelling of subevents as point sources.

in Figure 4.3 (kinematic modelling of subevents) and Figure 4.4 (subevents are modelled as point sources). These pictures show composite spectra for one realization of FSSD. 1D velocity model used here has 10 layers with $v_S = 400\,ms^{-1}$ in the top layer, mainfault size is $20 \times 25\,km$, primary grid size is $24 \times 28\,km$, rupture velocity is $v_r = 3000\,ms^{-1}$. Station is placed on the surface with epicentral distance equal to $11\,km$. In case of kinematic modelling of subevents, computation was made for both fixed and frequency dependent sampling and for two values of k ($k = 6$ and $k = 12$) getting identical results for all four cases. Hence, $k = 6$ and frequency dependent sampling performed well in this special case. We can see that calculation is surely correct up to $1\,Hz$ for 25×25 Green's function in primary grid (that is determined from fact, that the spectra for 25×25 and 20×20 Green's function in primary grid coincidence up to 1Hz approximately, see Figure 4.3 and Figure 4.4).

Chapter 5

Applications

5.1 Athens 1999 earthquake

Strong motion modelling, using composite model described in section 3.3, was performed on the Athens 1999 earthquake ($M_w = 5.9$). The choice of this event was not random. Other methods were developed at the time at our department and Athens 1999 earthquake was suggested for comparison. The source parameters (Table 5.1) were taken from Zahradník and Tselentis (2001). 1D model used for computation of impulse responses was taken from Novotný et al. (2001). Subevents were modelled as point sources (see section 4.2). The choice of characteristic dimension R was not problem here because the mainfault is nearly square (see Table 5.1), particularly we put R equal to the subevent's length L^j. The value $a = 1$ (see section 4.2) was preferred following Zahradník and Tselentis (2001). The rupture starts at the western bottom corner (38.08° N, 23.58° E, depth 12000 m) and spreads radially with constant rupture velocity. The parameters of FSSD are in Table 5.2. It is exactly FSSD shown in Figure 3.3. The only reason for such choice of FSSD was relatively high value of M. The calculation was made up to 6 Hz. One can see, that choice of point source approximation for bigger subevents is discussable, so using kinematic modelling would be more appropriate here. The computation was performed for 56 receivers placed on four concentric circles with center in the epicenter of the mainshock and with radius ranges from 5 km to 20 km. The results (see Figure 5.2) are PGA maps computed for 100 realizations of FSSD. By one realization of FSSD we mean, one realization of spatial distribution of set

$strike$	135°
dip	55°
$rake$	−84°
M_o^m	$7.8\,10^{17}\,Nm$
L^m	$7500\,m$
W^m	$6000\,m$
$\langle u^m \rangle$	$0.55\,m$
v_r	$2800\,ms^{-1}$
f_c^m	$0.37\,Hz$

Table 5.1: Basic source parameters of the Athens 1999 earthquake ($M_w = 5.9$).

j	1	2	3	4	5	6
N_j	1	4	16	68	271	1156
$L_j\,(m)$	3000	1500	750	375	188	94
$f_c^j\,(Hz)$	0.93	1.87	3.73	7.5	14.93	29.87

Table 5.2: Parameters of applied FSSD.

of subevents given by Table 5.2. By PGA we mean just absolute maximum from all three components of given accelerogram.

However, missing instruments in the near-field source region make the comparison with data hard. Especially, in the region with major damages no strong motion measurements are available. Thus the only information about strong ground motion at these locations is from macroseismic intensities published by NOA (see Figure 5.1). We can see that synthetic PGA maps (Figure 5.2) explain main features of macroseismic field (Figure 5.1). Maps of average PGA and maximum expectable PGA can be interpreted as a prediction tool. On the other hand, map generated for one realization of FSSD can be compared with observed macroseismic intensities. Proposed standard deviations $\sim 25\%$ (see Figure 5.2) seem to be reasonable.

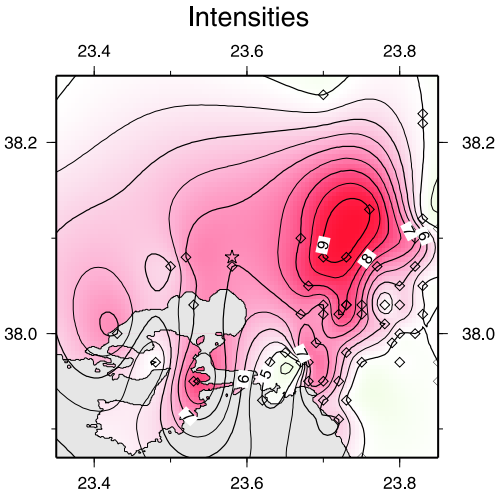

Figure 5.1: Macroseismic intensities published by NOA. Star denotes epicenter. Diamonds denote places where the macroseismic data were collected.

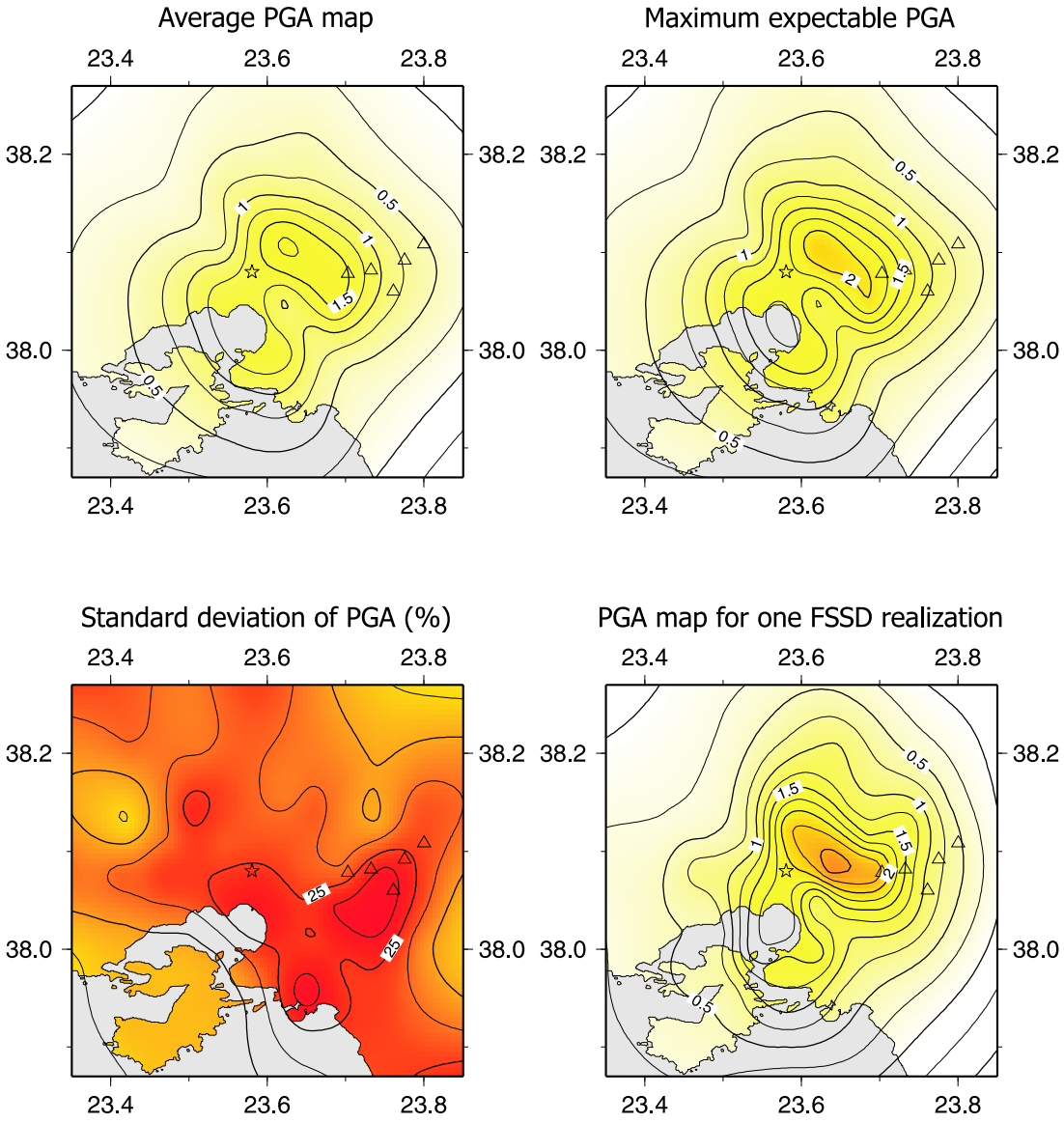

Figure 5.2: The results for Athens 1999 earthquake. PGA are carried out in ms^{-2}, standard deviations in percentage. Star denotes epicenter, triangles denote villages with major damage. Average PGA map show exactly the average of 100 realization of FSSD. Maximum expectable PGA map show the sum of average PGA and standard deviation of PGA (in ms^{-2}). Last map shows PGA computed for one realization of FSSD.

Chapter 6

Discussion and Conclusions

The composite source model with fractal subevent size distribution described above, represents reliable seismic source model for strong ground motion modelling for frequencies $f > 1Hz$, removing amplitude discrepancies in middle frequencies spectral levels. However, there is clear deficiency at low frequencies, indicating need of hybrid schemes presented by Kamae et al. (1998) and Hartzell et al. (1999). Hybrid schemes combine kinematic approach (used to model low frequency part) with composite approach (used to model middle and high frequency part). Hybrid schemes seem to be most successful in strong ground motion modelling, at the time (see Hartzell et al. (1999)). So the method is worth to be implemented into our model.

Fractal dimension D, characterizing generally any fractal distribution, is in our case determined (following Frankel (1991)) just from stress drop scaling. Constant stress drop scaling cause $D = 2$. Irikura and Kamae (1994), Zeng et al. (1994) and Hartzell et al. (1999), all of these were using $D = 2$, however, they came to this value in different way (they used exactly (3.27)), which is from our point of view less rigorous. We do not consider formula (3.27) to be generally correct in case of non-overlapping subevents fully filling up the mainfault.

We have described algorithm of generation of FSSD for practical use. The source code of FORTRAN 90 subroutine FRACTAL, generating such spatial distributions of subevents, is part of the thesis (Appendix). Hence, FSSD can be implemented easily by anyone who is interested in.

The favorable feature of FSSD is incorporation of final slip spatial variations over the mainfault. The fact that non-equal subevents produce inhomogeneous slip was firstly found out by Zeng et al. (1994). We have further showed, that our implementation of FSSD with fractal dimension $D = 2$ produces k^{-2} slip distribution, which is in agreement with recent source inversions (Mai and Beroza (2001)). That invokes the idea of well constrained future seismic source inversion, using our implementation of FSSD.

Although our study was focused on composite source modelling, we partially came in touch with kinematic source modelling, proposing some improvements, which may speed up computations significantly. Particularly, we proposed frequency dependent sampling together with interpolation of impulse responses over the mainfault.

Finally, the application on Athens 1999 earthquake showed capabilities of FSSD composite model combined with synthetically computed subevents. The generated PGA maps are in agreement with maps presented by Zahradník and Tselentis (2001). However, PGA maps represent only one of the results usable for engineering applications. Maps of durations, averaged PSA spectra and others indicators can be implemented easily.

One who is interested in strong motion modelling surely missed the term directivity in the whole study. We didn't mentioned it, because we had not studied this effect systematically. However looking at the PGA maps generated for Athens 1999 earthquake and take into account geometry of the faulting, especially position of hypocenter, one has to say that directivity is present. Unless a robust synthetic study is made, we would not rather discus the rate of directivity with respect to frequency.

Appendix

Subroutine FRACTAL

Here we provide subroutine FRACTAL, which generates in 1^{st} step N_i and R_i (see section 3.2) and in 2^{nd} step put the subevents randomly on the mainfault so they do not overlap with each other. The code is also available with more detail description on e-mail address: `burjanek@karel.troja.mff.cuni.cz`. The author appreciate your comments. In case of using the subroutine, please refer to:

Burjánek, J.: A composite source model with fractal subevent size distribution, Master Thesis, Dept. of Geophysics, Charles University, Prague, May 2002.

Subroutine FRACTAL is programmed in FORTRAN 90. It needs function RAN2 from Press et al. (1992) or some other generator of random numbers from interval $\langle 0, 1\rangle$ with uniform probability density function. An output is file SUBXY.DAT, which has following format:

1.line:	R_{main}/R_{min}	R_{main}/R_{min}		
2.line:	M			
3.line:	N_1	N_2	...	N_M
4.line:	R_1/R_{min}	R_2/R_{min}	...	R_M/R_{min}
5.line:	x_1+1	y_1+1	x_2	y_2
$\vdots$	$\vdots$	$\vdots$	$\vdots$	$\vdots$
X.line:	x_1+1	y_1+1	x_2	y_2

where R_{main}, R_{min}, M, R_i and N_i were defined in section 3.2 and $X = \sum_{i=1}^{m} N_i + 4$. x_1, y_1 are coordinates of left upper corner and x_2, y_2 are coordinates of right bottom corner of appropriate subevent.

```
module spol
  logical test
  integer, allocatable :: subxy(:,:)
  integer citac
  integer sublenx,subleny,xo,yo
end module

subroutine FRACTAL(nsubtypes,mainsize,lmax,idum)

! INPUT PARAMETERS:
! nsubtypes - number of the subevents types (in the text is denoted m)
! mainsize - determines R_main/R_min (see text, section 3.1.1)
! lmax - determines R_max/R_min (see text, section 3.1.1)
! idum - this is seed of random generator
!
! OUTPUT:
! output of subroutine fractal is file SUBXY.DAT (described in Appendix A)

use spol

integer nsubtypes
real*8, parameter :: lmin=1.d0
real*8 mainsize,lmax
integer, allocatable :: fault(:,:)
real*8, allocatable :: rfault(:,:)
integer nsub(nsubtypes),np
integer nsubsize(nsubtypes,2)
real*8 subsize(nsubtypes,2),c
real*8 deltax(nsubtypes)
real*8 koef,rsub(nsubtypes),area
real*8 pom
real*4 ra
integer idum

c=1.98d0

np=int(mainsize/lmin)-1
allocate(fault(0:np,0:np))
allocate(rfault(0:np,0:np))

open(4,status='replace',form='formatted',file='subxy.dat')

subsize=0.d0

do i=1,nsubtypes
  if (c/=1.d0) then
    deltax(i)=(c**(i-1))*(lmax-lmin)/(((c**nsubtypes)-1)/(c-1.d0))
  else
    deltax(i)=(lmax-lmin)/nsubtypes
  endif
  if (i/=1) then
    subsize(i,:)=subsize(i-1,:)+deltax(i-1)
  else
    subsize=lmin
  endif
enddo

koef=0.d0
do i=1,nsubtypes
  koef=koef+deltax(i)/subsize(i,1)
enddo

rsub=((mainsize**2)/(subsize(:,1)**3))*deltax(:)/koef
nsub(:)=nint(rsub(:))
nsubsize=nint(subsize/lmin)

do j=nsubtypes,2,-1
  area=(rsub(j)-dfloat(nsub(j)))*subsize(j,1)**2+(subsize(j,1)**2-dfloat(nsubsize(j,1))**2)*dfloat(nsub(j))
  rsub(j-1)=rsub(j-1)+area/(subsize(j-1,1)*subsize(j-1,2))
  nsub(j-1)=nint(rsub(j-1))
enddo

allocate(subxy(sum(nsub),4))
fault=0
subxy=0
citac=0
xo=0
yo=0
do i=nsubtypes,2,-1
  do j=1,nsub(i)
    citac=citac+1
    test=.TRUE.
    sublenx=np+1
    subleny=np+1
    do while (test)
      do while (((sublenx+xo)>np))
        ra=ran2(idum)
```

```
        xo=nint(dfloat(ra)*mainsize)
        sublenx=nsubsize(i,1)-1
      enddo
      do while (((subleny+yo)>np))
        ra=ran2(idum)
        yo=nint(dfloat(ra)*mainsize)
        subleny=nsubsize(i,2)-1
      enddo
      test=.FALSE.
      call control()
      if (test) then
        sublenx=np+1
        subleny=np+1
      endif
    enddo
    fault(xo:(xo+sublenx),yo:(yo+subleny))=i-1
    subxy(citac,1)=xo
    subxy(citac,2)=yo
    subxy(citac,3)=xo+sublenx
    subxy(citac,4)=yo+subleny
  enddo
enddo

do j=0,np
  do i=0,np
    if (fault(j,i)==0) then
      citac=citac+1
      subxy(citac,1)=j
      subxy(citac,2)=i
      subxy(citac,3)=j
      subxy(citac,4)=i
    endif
    rfault(j,i)=dfloat(fault(j,i))
  enddo
enddo

l=sum(nsub)
write(4,*) np+1, np+1
write(4,*) nsubtypes
do i=1,nsubtypes/2
  pom=nsub(i)
  nsub(i)=nsub(nsubtypes+1-i)
  nsub(nsubtypes+1-i)=pom
  pom=subsize(nsubtypes+1-i,1)
  subsize(nsubtypes+1-i,1)=subsize(i,1)
  subsize(i,1)=pom
enddo
nsubsize=int(subsize)
write(4,*) nsub
write(4,*) nsubsize(:,1)
do i=1,l
  write(4,*) subxy(i,:)+1
enddo

deallocate(subxy)
deallocate(fault)
deallocate(rfault)
close(4)

end subroutine

subroutine control()
use spol

do m=1,citac-1
  if (((xo>=subxy(m,1)).AND.(yo>=subxy(m,2))).AND.((xo<=subxy(m,3)).AND.(yo<=subxy(m,4)))) test=.TRUE.
  if (((xo+sublenx>=subxy(m,1)).AND.(yo>=subxy(m,2))).AND.((xo+sublenx<=subxy(m,3)).AND.(yo<=subxy(m,4)))) test=.TRUE.
  if (((xo+sublenx>=subxy(m,1)).AND.(yo+subleny>=subxy(m,2))).AND.((xo+sublenx<=subxy(m,3)).AND.(yo+subleny<=subxy(m,4)))) test=.TRUE.
  if (((xo>=subxy(m,1)).AND.(yo+subleny>=subxy(m,2))).AND.((xo<=subxy(m,3)).AND.(yo+subleny<=subxy(m,4)))) test=.TRUE.
enddo

end subroutine
```

References

Aki, K., and P.G. Richards, *Quantitative Seismology: Theory and Methods*, W.H. Freeman and Company, New York, 1980.

Andrews, D.J., A stochastic fault model, 1, Static case *J. Geophys. Res., 85*, 3867-3877, 1980.

Beresenev, I.A., and G.M. Atkinson, Modeling finite-fault radiation from the ω^n spectrum, *Bull. Seism. Soc. Am., 87*, 67-84, 1997.

Beresnev, I.A., and G.M. Atkinson, FINSIM - a FORTRAN program for simulating stochastic acceleration time histories from finite faults, *Seism. Res. Lett 69*, 27-32 1998.

Bernard, P., A. Herrero, and C. Berge, Modeling directivity of heterogenous earthquake ruptures, *Bull. Seism. Soc. Am., 86*, 1149-1160, 1996.

Boatwright, J., The dynamic models for far-field acceleration, *Bull. Seism. Soc. Am., 72*, 1049-1068, 1982.

Boatwright, J., The seismic radiation from composite models of faulting, *Bull. Seism. Soc. Am., 78*, 489-508, 1988.

Boore, D. M., Stochastic simulation of high-frequency ground motions based on seismological models of the radiated spectra, *Bull. Seism. Soc. Am. 73*, 1865-1894, 1983.

Bouchon, M., A simple method to calculate Green's functions for elastic layered media, *Bull. Seism. Soc. Am. 71*, 959-971, 1981.

Brune, J., Tectonic stress and the spectra of seismic shear waves from earthquakes, *J. Geophys. Res., 75*, 4997-5009, 1970 (correction,*J. Geophys. Res., 76*, 5002, 1971).

Coutant, O., Program of Numerical Simulation AXITRA. Res. Report LGIT, Grenoble, 1989, (in French).

Frankel, A., High-frequency spectral fall-off of earthquakes, fractal dimension of complex rupture, b value, and the scaling strength on faults, *J. Geophys. Res., 96*, 6291-6302, 1991.

Frankel, A., Simulating strong motions of large earthquakes using recordings of small earthquakes: the Loma Prieta mainshock as a test case, *Bull. Seism. Soc. Am., 85*, 1144-1160, 1995.

Hanks, T.C., b values and $\omega^{-\gamma}$ seismic source models: Implications for tectonic stress variations along active crustal fault zones and the estimation of high-frequency strong ground motion, *J. Geophys. Res., 84*, 2235-2242, 1979.

Hartzell, S., Earthquake aftershocks as Green's functions *Geophys. Res. Lett. 5*, 1-4, 1978.

Hartzell, S., S. Harmsen, A. Frankel, and S. Larsen, Calculation of broadband time histories of ground motion: comparsion of methods and validation using strong-ground motion from the 1994 Northridge earthquake, *Bull. Seism. Soc. Am., 89*, 1484-1504, 1999.

Hisada, Y., A theoretical omega-squared model considering the spatial variation in slip and rupture velocity, *Bull. Seism. Soc. Am., 90*, 387-400, 2000.

Hisada, Y., A theoretical omega-squared model considering the spatial variation in slip and rupture velocity. Part 2: Case for a two-dimensional source model, *Bull. Seism. Soc. Am., 91*, 651-666, 2001.

Irikura, K., and K. Kamae, Estimation of strong ground motion in broad-frequency band based on seismic source scaling model and an empirical Green's function technique, *Annali Di Geofisica 37*, 1721-1743, 1994.

Joyner, W.B., and D.M. Boore, On simulating large earthquakes by Green's function addition of smaller earthquakes, in *Earthquake Source Mechanics*, edited by S. Das, J. Boatwright, and C.H. Scholz (AGU, Geoph. monogr. 37, M. Ewing vol.6), 269-274, 1986.

Kamae, K., K. Irikura, and A. Pitarka, A technique for simulating strong ground motion using hybrid Green's function, *Bull. Seism. Soc. Am., 88*, 357-367, 1998.

Kanamori, H. and D.L. Anderson, Theoretical basis of some empirical relations in seismology, *Bull. Seism. Soc. Am., 65*, 1073-1096, 1975.

Kostrov, B.V., and S. Das, *Principles of Earthquake Source Mechanics*, Cambridge Univ. Press, Cambridge, UK, 1988.

Lee, Y.W., *Statistical Theory of Communication*, John Wiley and Sons, Inc., New York, 1960.

Lay, T. and T.C. Wallace, *Modern Global Seismology*, Academic Press, San Diego, 1995.

Mai, P.M., and G.C. Beroza, A spatial random-field model to characterize complexity in earthquake slip, *submitted to J. Geophys. Res.*, 2001.

Novotný, O., J. Zahradník, and G-A. Tselentis, North-Western Turkey earthquakes and the crustal structure inferred from surface waves observed in Western Greece, *Bull. Seism. Soc. Am., 91*, 875-879, 2001.

Press, W.H., S.A. Teukolsky, W.T. Vetterling, B.P. Flannery, *Numerical recipes in FORTRAN : the art of scientific computing*, Cambridge Univ. Press, Cambridge, UK, 1992.

Somerville, P., K. Irikura, R. Graves, S. Sawada, D. Wald, N. Abrahamson, Y. Iwasaki, T. Kagawa, N. Smith, A. Kowada, Characterizing crustal earthquake slip models for the prediction of strong ground motion, *Seism. Res. Lett 70*, 59-80, 1999.

Tumarkin, A.G., and R.J. Archuleta, Empirical ground motion prediction, *Annali Di Geofisica 37*, 1691-1720, 1994.

Turcotte, D.L., Fractals in geology and geophysics, *Pure. Appl. Geophys., 131*, 171-196, 1989.

Wessel, P., W.H.F. Smith, Free Software Helps Map and Display Data. *EOS Trans. AGU, 72*, 441, 445-446, 1991.

Zahradník, J., G-A. Tselentis, Modeling strong-motion accelerograms by PEXT method, application to the Athens 1999 earthquake, *submitted* 2001.

Zeng, Y., J.G. Anderson, and G. Yu, A composite source model for computing synthetics strong ground motions, *Geophys. Res. Lett. 86*, 725-728, 1994.

Zeng, Y., and J.G. Anderson, A composite source model of the 1994 Northridge earthquake using genetic algorithms, *Bull. Seism. Soc. Am., 86*, S71-S83, 1996.